3-29-2018

Identifying the Origins of Volcanic Ash Deposits Using Their Chemical and Physical Compositions

Emmanuel Soto
Florida International University, esoto033@fiu.edu

DOI: 10.25148/etd.FIDC006542

FLORIDA INTERNATIONAL UNIVERSITY

Miami, Florida

IDENTIFYING THE ORIGINS OF VOLCANIC ASH DEPOSITS USING THEIR CHEMICAL AND PHYSICAL COMPOSITIONS

A thesis submitted in partial fulfillment of

the requirements for the degree of

MASTER OF SCIENCE

in

GEOSCIENCES

by

Emmanuel Soto

2018

To: Dean Michael R. Heithaus
College of Arts, Sciences and Education

This thesis, written by Emmanuel Soto Esguerra, and entitled Identifying the Origins of Volcanic Ash Deposits Using Their Chemical and Physical Compositions, having been approved in respect to style and intellectual content, is referred to you for judgment.

We have read this thesis and recommend that it be approved.

_____
Laurel Collins

_____
Grenville Draper

_____
Rosemary Hickey-Vargas, Major Professor

Date of Defense: March 29, 2018

The thesis of Emmanuel Soto Esguerra is approved.

_____
Dean Michael R. Heithaus
College of Arts, Sciences and Education

_____
Andrés G. Gil
Vice President for Research and Economic Development
and Dean of the University Graduate School

Florida International University, 2018

DEDICATION

I dedicate this Thesis to my parents, for all their love and support.

ACKNOWLEDGMENTS

First, I would like to thank my academic advisor, Dr. Rosemary Hickey-Vargas for her kindness, wisdom, and guidance from the very beginning to the end. I will forever be grateful you chose me as your student. Secondly, to the members of my committee for accepting their role and for challenging my work whenever necessary. Lastly, I would like to thank my life partner Adhly Huertas, for her understanding, patience, and motivation throughout this journey. Without her contribution, this work might have never been finished. I also thank Tom Beasley, of FIU's Florida Center for Analytical Electron Microscopy, and Dr. Sarah Jantzi, of FIU's Trace Evidence Analysis Facility, for instruction and assistance with chemical analyses.

I have found my coursework throughout the Curriculum and Instruction program to be stimulating and thoughtful, providing me with the tools with which to explore both past and present ideas and issues.

ABSTRACT OF THE THESIS

IDENTIFYING THE ORIGINS OF VOLCANIC ASH DEPOSITS USING THEIR CHEMICAL AND PHYSICAL COMPOSITIONS

by

Emmanuel Soto

Florida International University, 2018

Miami, Florida

Professor Rosemary Hickey-Vargas, Major Professor

Pleistocene-Recent ocean sediments collected offshore Chile by Ocean Drilling Program Leg 202 contained layers of volcanic ash of unknown origin. These deposits may have originated from sources in the Southern Volcanic Zone (SVZ) within the Andean Volcanic Belt to the east, or from explosive volcanoes in the southwestern Pacific transported by westerly prevailing winds. In this study, mineral and glass textures and compositions of Leg 202 ashes were evaluated to try to determine the sources of the ash layers. Ash fragments were imaged and analyzed for major elements using an SEM with X-Ray detector and for trace elements using LA-ICPMS. Results show that the ash samples are rhyolitic and that they formed in a subduction zone setting or a continental margin. The ash samples have distinct physical and geochemical features that can be used in the future to identify their source(s) by comparison to databases of Pleistocene-Recent explosive volcanic eruptions.

TABLE OF CONTENTS

CHAPTER PAGE

LIST OF TABLES

TABLES PAGES

LIST OF FIGURES

FIGURES PAGES

ABBREVIATIONS AND ACRONYMS

APC	Advance Piston Corer
AVZ	Austral Volcanic Zone
Ba	Barium
BHA	Bottom Hole Assembly
BHVO-2	Basalt, Hawaiian Volcanic Observatory-2
BSE	Bulk Silicate Earth
BSE	Backscattered Electrons
Ca	Calcium
Ce	Cerium
CSVZ	Central Southern Volcanic Zone
CVZ	Central Volcanic Zone
Dy	Dysprosium
EDS	Energy Dispersive System
EPMA	Electron Probe Micro-Analyzer
Eu	Europium
Fe	Iron
Gd	Gadolinium
GVP	Global Volcanic Program
Hf	Hafnium
HFSE	High field strength element
HREE	Heavy rare earth elements
IEDA	Integrated Earth Data Applications

IODP	International Discovery Program
Ka	Kiloannus
La	Lanthanum
LA ICP-MS	Laser Ablation Inductive Coupled Plasma Mass Spectrometry
LaMEVE	Large Magnitude Explosive Volcanic Eruptions
LILE	Large-ion lithophile element
LREE	Light rare earth element
Ma	Mega-annum
Nb	Niobium
Nd	Neodymium
NSVZ	Northern Southern Volcanic Zone
NVZ	Northern Volcanic Zone
ODP	Ocean Drilling Program
PCC	Puyehue Cordon-Caulle
Rb	Rubidium
RGM	Rhyolite, Glass Mountain
SE	Secondary Electrons
SEM	Scanning Electron Microscope
Sr	Strontium
SSVZ	Southern Southern Volcanic Zone
SVZ	Southern Volcanic Zone
Th	Thorium
Ti	Titanium

TSVZ	Transitional Southern Volcanic Zone
USGS	United States Geological Survey
VEI	Volcanic Explosivity Index
XCB	Extended Core Barrel
Y	Yttrium
Yb	Ytterbium
Zr	Zirconium

INTRODUCTION

Volcanic ash is the finer (under 2mm) particulate material ejected during a volcanic eruption. It is mainly composed of volcanic glass fragments, along with mineral grains and lithic grains. The eruption column, a cloud of volcanic ash, can rise over 40 km, reaching the stratosphere where it can create short term climatic changes (Prata et al., 2007). Clouds formed by volcanic ash can become a serious security risk to air transportation since they do not appear on radar and look similar to weather clouds (Roth and Guritz, 1995). The volcanic eruption from Mount Redoubt in 1989 caused a plane crash when a passenger jet flew through the ash cloud and experienced complete engine failure.

Volcanic ash can have a large impact on the climate and biogeochemical processes as it can absorb infrared light differently from water and ice. Volcanic ash can also alter the chemistry, cloudiness, and radiation budget of the atmosphere for a few weeks (Niemeier et al., 2009). Once in the atmosphere, wind patterns can carry the ash over great distances, making it difficult to identify their origin (Figure 1). Large explosive eruptions have the potential to cover continental scale areas with ash (Baines and Sparks, 2005). Well-preserved volcanic ash sediments in the geological record represent an invaluable reconstruction tool for past eruptions in any given location. Ash also provides key stratigraphic markers for paleoenvironmental studies, and aids with the investigation of volcanic eruption impacts on the environment (Carel et al., 2011). For analytical purposes, the ideal location in which volcanic ash can be found is within

oceanic sediments on the ocean floor, unlike terrestrial fallout deposits, it is rarely disrupted (Keller et al., 1978). As a key indicator of geologic history, volcanic-ash layers found in oceanic sediments are among the most well preserved stratigraphic markers known today (Carel et al., 2011). Not only are they important chronological tools when dated radiometrically, volcanic-ash layers can also provide us with information about past climatic events (Bard et al., 1994). Oceanic sediments can be dated using marine biostratigraphy, which is the use of fossils of marine organisms to identify time intervals. A specific organism can provide the information needed to place a sediment into age brackets. In some cases, minerals in the ash can be dated radiometrically (Turner et al., 1980).

The study of volcanic activity in the Southern Volcanic Zone is of great importance due to the limited amount of data available for the chemical composition of different eruption points. Although the Chilean's active margins have been studied extensively, large gaps of information are still missing. Many volcanic eruptions in the Andes from different time periods have not been geochemically recorded, which creates large gaps in the literature. This makes it harder to locate the origin of an unknow sample of volcanic ash. This project aims to contribute a significant amount of data which can be of use in future studies.

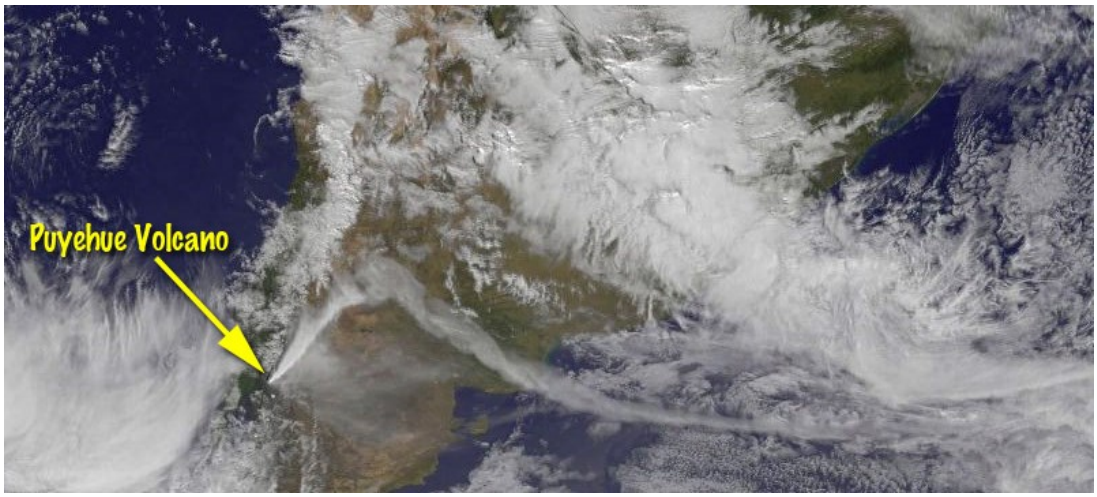

Figure 1. Eruption from the Puyehue-Cordon Caulle Volcano in Chile taken 06/06/11. Picture taken via satellite by NASA.

Expedition 202 of the Oceanic Drilling Program

In the present study, volcanic ash was found in oceanic sediments off the coast of Chile in areas with sedimentation rates of 80-2000 m/m.y. (Mix et al., 2003a), in close proximity to the Andean Southern Volcanic Zone (SVZ). The ash samples were uncovered in the year 2002 by the Ocean Drilling Program (ODP), now known as the International Ocean Discovery Program (IODP); (Figure 2). The IODP is an international research consortium that studies oceanographic and earth science problems by drilling and analyzing rock cores and sediments from the ocean floor (Anonymous, 2007). The expedition had a total of eleven drill sites in the Southeast and Equatorial Pacific, of which, four were near the SVZ. These four sites had a total of fifteen ash layers divided amongst them, one ash layer was chosen per site. This was based on factors such as thickness (the selected ash layers were at least half an inch thick) and depth (layers at similar depths). The four drill sites (1232, 1233, 1234, and 1235) located west of the Andes had a depth range of 120-360m, and basal ages from 0.26-1.69 Ma, which places them in the Pleistocene to Recent.

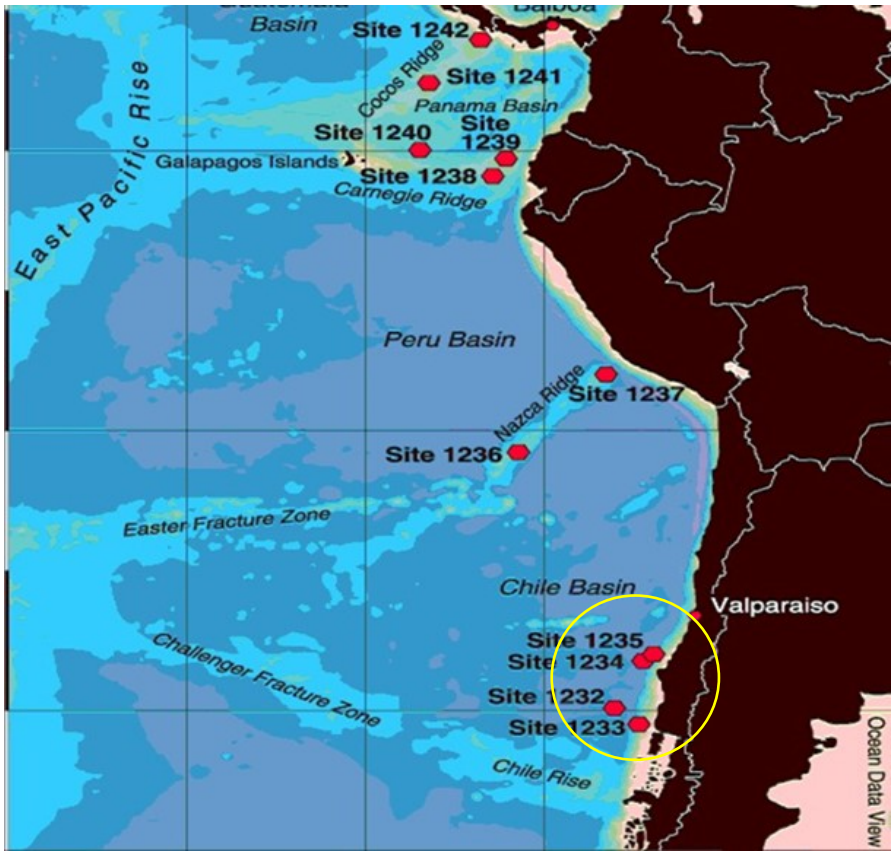

Figure 2. Drill sites from the ODP Expedition 202. Sites 1232, 1233, 1234, and 1235 all contained ash layers and are in close proximity to the Southern Volcanic Zone. Image taken from the ODP expedition 202 log.

Site 1232A is located in the Chilean basin, between the Mocha and the Valdivia fracture zones. The major grain composition of this site is siliciclastic silty clay in a record dominated by turbidite deposits. This late Pleistocene sequence is 390.6 meters composite depth thick, with a basal age of 0.78 Ma (Mix et al., 2003b). Site 1233C is located in a small forearc basin on the continental slope, shoreward of the Chile trench, at a water depth of 838m. According to ODP researchers, the volcanic ash layers on this site consist of 95% unaltered volcanic glass to acidic to intermediate composition. The mineral composition consists of plagioclase, quartz, biotite, and small amounts pyroxene. The ash layers with intermediate composition contain labradorite plagioclase, less quartz

and biotite, and has abundant pyroxenes. The layers were created during periods of high sedimentation rates ranging from 11 to 170 cm/Ka during the Holocene epoch. The presence of *E. huxleyi*, a unicellular, eukaryotic phytoplankton at the bottom of the hole indicates that the entire sequence is younger than 260 Ka (Mix et al., 2003b). Site 1234A is located on a flat bench of the continental slope, around 60 km shoreward of the Peru-Chile trench. At this site, thin silt-rich layers and volcanic ash layers are present as minor lithologies. The basal age of the sequence is less than 0.26 Ma, but no age model was created because of the very high sedimentation rates and low datum count (Mix et al., 2003b). Site 1235 is located on a sloping terrace on the upper continental slope, with a 5-cm-thick layer of pale ash recovered that represents the third minor lithology of the core. The mineral composition of the volcanic glass shards shows minor amounts of labradoritic plagioclase and trace amounts of quartz, mica, hornblende, and orthopyroxene (Mix et al., 2003b).

As a consequence of the proximity of the drill site to the SVZ and the Pleistocene-Recent volcanic activity of this area, it can be hypothesized that the volcanic ashes originated somewhere in the SVZ. However, numerous other explosive volcanic centers with Pleistocene-recent activity are located at similar latitudes in the southern hemisphere. On the basis of the great distance of transport inferred for some eruptions (Baines and Sparks, 2005, Fig. 1) and the overall westerly prevailing wind direction at this latitude (Moreno et al., 2007) it is also possible that the ashes originated at another location. The overall purpose of this research is to provide information bearing on the origin of the ash layers at ODP Sites 1232, 1233, 1234, and 1235.

Geologic Setting

The Andean Southern Volcanic Zone

Andean volcanic activity is created by the subduction of the Nazca and the Antarctic oceanic plates under the less dense continental lithosphere of western South America (Moreno et al., 2007). The tectonic activity has created more than 200 Pleistocene-Recent arc volcanoes which are divided into four zones: The Northern Volcanic Zone (NVZ), the Central Volcanic Zone (CVZ), the Southern Volcanic Zone (SVZ), and the Austral Volcanic Zone (AVZ), all together, they make up the Andean volcanic arc. The Southern Volcanic Zone (33°S and 46°S) is made up of rhyolitic to andesitic volcanic products dating back to before the Pliocene, which in turn are underneath Plio-Quaternary volcanoes. (Moreno et al., 2007). The volcanoes are composed of basaltic through rhyolitic rocks and tephra and reach elevations of over 6000m. The SVZ chain of volcanoes is located at the border between Chile and Argentina and has more than 70 Pleistocene-Recent stratovolcanoes in Chile alone. The SVZ continues to be a high-volcanic-activity area, with up to one eruption per year on average for the last 15,000 years (Moreno et al., 2007). Volcanoes in this area are mainly calc-alkaline, containing high alumina basalts and andesites (Carel et al., 2011).

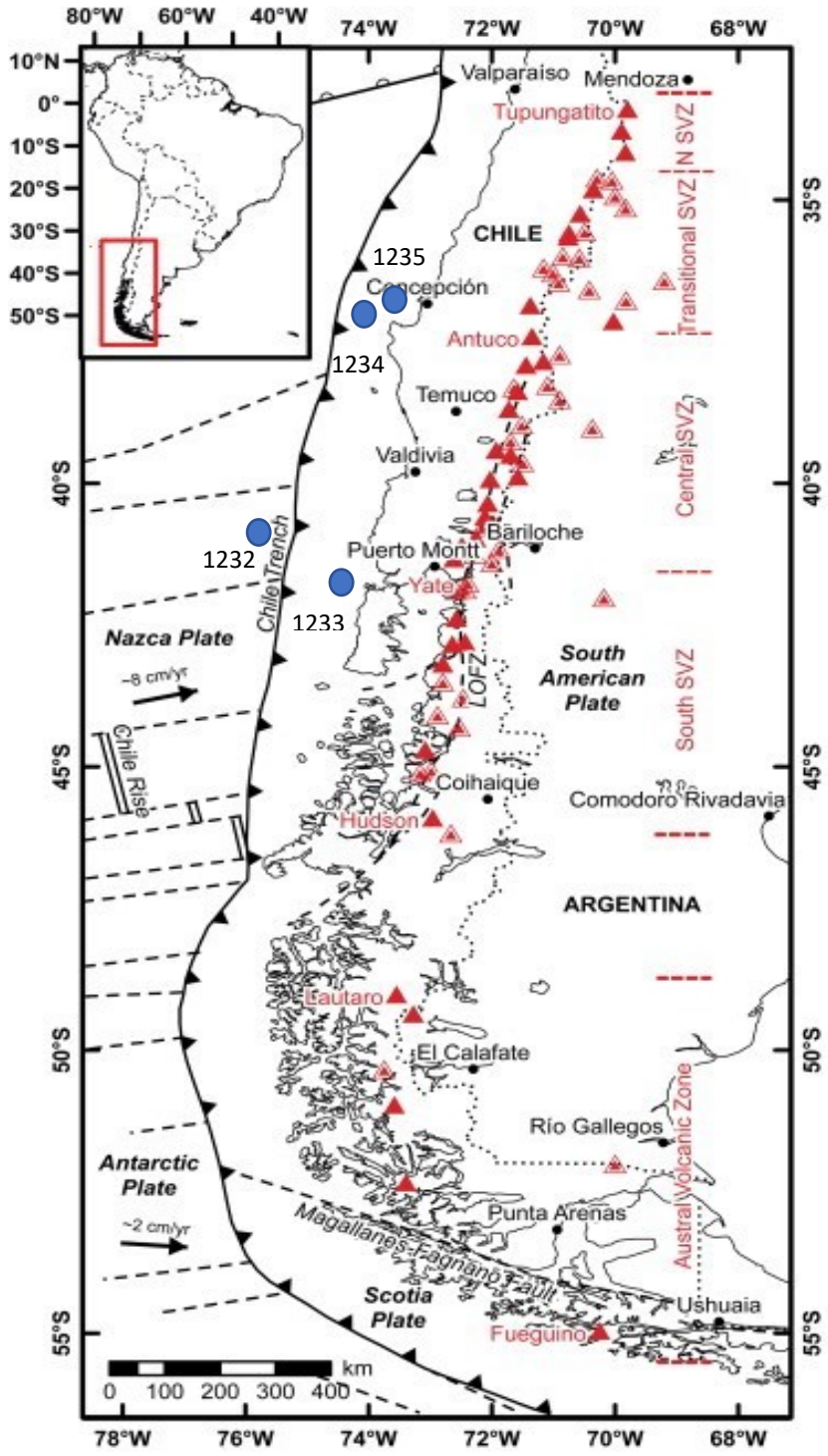

Figure 3. Map of Southern Chile showing the divisions of the Andean SVZ. Blue circles indicate the location of each Site (Fontijn et al., 2014).

The Pleistocene and Holocene volcanoes of the SVZ are divided into four different segments on the basis of petrologic and geochemical considerations, as well as tectonic movements (Moreno et al., 2007, Figure 3). These are the Northern SVZ (33.3°S–34.4°S), the Transitional SVZ (34.4°S–37°S), the Central SVZ (CSVZ; 37°S–42°S) and the Southern SVZ (SSVZ: 42°S–46°S). The NSVZ has eight composite stratovolcanoes and the giant Diamante caldera. During the Pleistocene and Holocene, the NSVZ had relative low rate of magmatic extrusion from stratovolcanoes, with the largest being Marmolejo (Moreno et al., 2007). The TSVZ shows the arc widening considerably eastward. The main features of this volcanic zone are compound stratovolcanoes and large volcanic complexes on top of old basaltic shield volcanoes. Giant calderas and volcanic fields are also present with some caldera systems producing large volumes of Pleistocene rhyolites, for example, the Descabezados-Quizapu-Cerro Azul, Laguna del Maule, and Calabozos volcanic fields which contain well over 200 vents (Moreno et al., 2007). The CSVZ is wide on its northern side until it reaches 39° S. It then narrows into a chain 80 km wide without intra-arc basins. The volcanic front of CSVZ has stratovolcanoes from the Pleistocene to Holocene which overlie eroded Pliocene and Pleistocene volcanic features. The CSVZ is an important volcanic zone, since it is the most volcanically active segment along the Andes with two of the most active volcanoes in South America, Llaima and Villarrica (Moreno et al., 2007). Because of its high volcanic activity, the sizes of the volcanoes (biggest in the SVZ), and their proximity to the eastern edge of the Central Valley, the CSVZ is considered an area of high volcanic risk. South of the CSVZ lies the SSVZ which consists of 13 Quaternary volcanoes of which, at least ten have had medium to large explosive eruptions during the

Holocene. The volcanic centers of the SSVZ are in general covered with snow a result caused by the cool climate and high precipitation. Melted snow during eruptions increases the chances of creating natural disasters around populated areas by forming lahars (Moreno et al., 2007).

Many eruptions in the SVZ have been explosive, with a high Volcanic Explosivity Index (VEI). Volcanoes Calabozos and Villarrica both had massive volcanic eruptions during the Pleistocene epoch with a Volcanic Explosivity Index (VEI) of 7 and 6, respectively (Smithsonian, 2011). The VEI is a measurement of the explosiveness of volcanic eruptions, a relative scale ranging from 1 to 8 that enables volcanic eruptions to be compared with one another by measuring the eruption cloud height, the volume of product ejected, and qualitative observations (Smithsonian, 2011). Eruptions that have a high VEI count (8 being the highest) produce massive amounts of volcanic-ash that can cover long distances extending all the way around the world. The high volcanic activity in the SVZ (Table 1, APPENDIX C), the high VEI count of eruptions, and the proximity to the location the ash samples were recovered favor the original source of the volcanic ashes to be somewhere in the SVZ. In contrast, wind patterns are not consistent with an origin for the ash in the SVZ. The trajectory of the prevailing winds in the Andes is from West to East in the Troposphere, as shown by the widespread deposition of Pleistocene-recent volcanic ashes from the SVZ to the East, in Argentina and the Atlantic Ocean (Fig. 1, Moreno et al., 2007). Therefore, it is also worth considering an origin at centers having explosive eruption elsewhere in the southern hemisphere such as the Okataina Volcanic Complex in the Taupo Volcanic Zone in New Zealand.

OBJECTIVE OF PROJECT

For the present research, I have chosen the uppermost (most recent) ash layer from each of ODP Sites 1232, 1233, 1234 and 1235. The objectives of this research are:

1) To determine whether the ash layers from the different sites originated from the same volcanic source or different ones.

2) To collect information that can be used to identify the source of the ashes, and, if possible, to identify that source or eruption.

The methods used to characterize the ash include detailed physical analysis of each sample, as chemical analyses of major and trace elements. Data were compared to those available in geologic databases such as Earthchem, LaMEVE, and the Smithsonian Institution Global Volcanism Program. Data on the physical and chemical properties of ash obtained in this study will also be contributed to these databases for use in volcanological studies.

METHODOLOGY

Sample collection and selection

For the purpose of this project, prepared samples were obtained from the International Oceanic Discovery Program. Core samples were collected during the 202 expedition by the Ocean Drilling Program (ODP) in 2002. Once an oil exploration vessel (Anonymous, 2007), in 1985, the JOIDES Resolution became a scientific research vessel

for the ODP. The vessel has a drilling capability of up to 8,385 m total depth. It is an outfitted drill ship that can be positioned over a specific seafloor location while drilling on the desired penetration level below the seafloor. The ship is equipped with laboratory rooms and equipment allowing core analysis and borehole data collection to be performed.

During expedition 202, oceanic sediments in the southwest and equatorial Pacific were collected (Mix et al., 2003a). The four sites nearest to the Andes, which are in the Chile Basin and the Chile Margin, have basal ages of 0.26-1.69 million years, which places them in the Pleistocene to Recent (Figure 4). For Site 1232A, a depth of 4,091.4m below the rig floor (mbrf) was established by the precision depth recorder measurement (Mix et al., 2003a). To drill the core, a 136m-long advance piston corer (APC) and an extended core barrel (XCB) bottom-hole assembly (BHA) were used. For Site 1233C the calculated seafloor recovery for the core was 848.7 mbsf (Mix et al., 2003a). Site 1234A had issues in many of its cores due to expanding gasses during recovery. This resulted in gas voids and expanding cores prior to processing. To relieve the gas pressure, holes were drilled into the cores before they were processed (Mix et al., 2003a). Site 1235B also underwent some complications. Core 19H received damage from deceleration forces created when the formation prevented a full stroke of the corer. Another issue with Site 1235B happened at Core 16H, where the liner was being cut into sections on the catwalk and it fragmented into pieces and the sediment exploded as a result of excessive of gas pressure (Mix et al., 2003a).

In total, fifteen volcanic ash layers were identified at the four sites, with varying thickness and depth. For my project, the uppermost layer from each site was analyzed, four in total. These are: Site 1232A (selected ash layer is in core 034X, section 03W, intervals 116-117), Site 1233C (core 002H, section 06W, intervals 76-77), Site 1234A (core 003H, section 03W, intervals 49-50), Site 1235B (core 014H, section 05W, intervals 120-121.5).

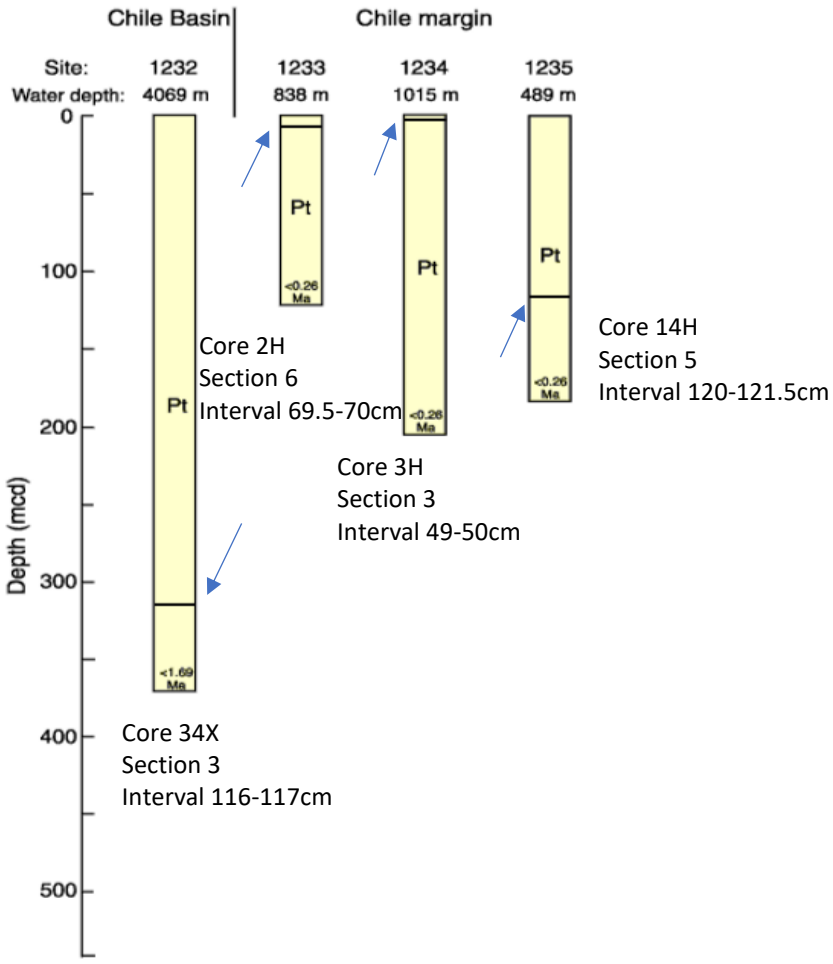

Figure 4. Depth and location of the four drill sites in expedition 202. Black lines indicate the location of the studied ash samples.

Laboratory Procedures

Sample Preparation

Before the chemical analysis, samples underwent a series of treatments. First, samples were wet sieved, to separate the fine and coarse grains using de-ionized water to break down agglomerates. For this project, two mesh sizes were utilized, 200 mesh (74 microns) and 120 mesh (125 microns). After wet sieving, the samples were oven-dried at 100 degrees C and labeled by size and origin. After the wet sieving process, the samples were placed in the ultrasonicator. This instrument is designed to remove unwanted material such as fossils from samples without compromising their physical properties. The samples were placed in a small glass bottle with de-ionized water and then closed. The ultrasonicator was filled with water and turned on for at least 20 minutes. If during this process, a substantial amount of residue was seen floating in the bottle, the process of ultrasonication could be repeated. After the samples were ultrasonicated, they are sieved one more time to ensure that only the clean particles, free of adhering materials are recovered.

Observation of Physical Properties

The morphology of glass shards (shape, vesicularity, color, and surface alteration) have proven to be useful identification tools (Turner et al., 2004). Glass shape measurements can aid in locating the origins of fragments and to predict particle behavior, such as scattering properties (Liu et al., 2015). Volcanic ash can be found in a diverse spectrum of shapes, each with different physical and chemical properties. The shapes of glass shards also reflect the fragmentation mechanisms that occur during an

eruption, which are controlled by magmatic properties (such as viscosity, temperature, chemical composition, and water content); (Liu et al., 2015).

Physical analysis was done through a transmitted light microscope for a primary assessment of the minerals and glass fragments present, their shape, and abundance. The morphology of the glass fragments was then described and photographed using both an optical digital camera and the Scanning Electron Microscope (SEM). The SEM is used to inspect samples at high magnifications using signals produced by the interaction between focused electrons and an area of the sample. The SEM uses an electron gun which shoots focused electrons on a fine beam. The interactions between the atoms of the sample and electron beam creates radiation products such as Backscattered Electrons and Secondary Electrons (SE) (Goldstein et al., 2003). The radiation product is collected by a detector which is then amplified, analyzed, and transformed into topographic images of the area's surface. Backscattered Electron are especially useful to distinguish one material from another because specimens with higher atomic numbers display higher brightness than specimens with smaller atomic numbers. Backscattered Electron images (APPENDIX B) will show compositional differences as well as glass orientation, both of which are important for physical analysis.

During the sample preparation process, glass samples (10 glass fragments per site) were collected and placed on a thin section with double-adhesive carbon tape for chemical analysis. An additional batch of samples was generated and carbon coated to

obtain images at high vacuum. Carbon coating is used to improve the imaging of samples. Creating a conductive layer of metal on the sample inhibits charging, reduces thermal damage while improving the secondary electron signal required for analysis in the SEM. Conductive fine carbon layers are needed for x-rays microanalysis.

Chemical Analysis of Glass Fragments

After the physical analysis, major and trace element analysis was performed on the selected individual glass shards from each interval. Major elements are those with concentrations greater than 2 wt%, while trace elements are present in concentrations below 0.1 wt% (Blatt et al., 2006). Petrologists have developed many chemical and mineral indices to categorize igneous rocks based on the fundamental patterns they show, for example, Harker diagrams showing two elements on x and y axes. Trace element concentrations for example can be very distinctive for igneous rocks and can provide a base line for comparison with a specific chemical reservoir (Blatt et al., 2006). The two most commonly used chemical reservoirs are the primordial earth modeled by chondritic meteorites (Sun, 1982), and the primordial mantle (McDonough and Sun, 1995; Sun and McDonough, 1989). The values in chondritic meteorites are chosen to normalize the standard because they provide relatively unfractionated samples of materials from the solar system and are commonly used as geochemical references in many studies. The primordial mantle approach is based on an estimate of the chemical composition of primitive mantle with bulk silicate earth (BSE). It uses compositional trends in upper mantle peridotites which are interpreted as melting trends. The primordial mantle is the preferred reference model because it is based on terrestrial samples that does not require

assumptions of the chemical composition of Earth but it incorporates cosmo-chemical data such as chondritic values for relative abundances (Lyubetskaya and Korenaga, 2007). In spider diagrams, the selected trace elements are plotted horizontally (in order of increasing atomic number) and the normalized element abundance is plotted vertically typically using a log scale for a smoother pattern (Blatt et al., 2006).

After performing chemical analysis on glass samples, data were plotted on Harker and spider diagrams, also known as a multi-element plots. These plots are useful in determining whether two or more ash layers from different sites originated from the same volcanic source.

Major element analysis was performed on glass shards using the EDS (Energy Dispersive X-ray) system of the Scanning Electron Microscope (SEM) JEOL JSM 5900LV in the Department of Earth and Environment at Florida International University (FIU). Backscattered images were also collected for the physical evaluation of the glass shards, providing important information regarding their homogeneity. Trace elements were analyzed using the Element 2 LA ICP-MS in the Department of Chemistry and Biochemistry at FIU. The compositional data for volcanic ashes contains major elements (>10,000 ppm) and trace elements (<10,000 ppm), with typical analyses for interpretation including 10 major elements (Si, Al, Fe, Mg, Ca, Na, K, Ti, P, and Mn), and 30 or more trace elements (Hickey-Vargas et al., 2016b). For the present project, 16 trace elements were analyzed (Ti, Ce, Nd, Gd, Dy, Hf, La, Ba, Zr, Nb, Rb, Sr, Yb, Th, Y, and Eu .

Figure 5 was created using the data collected from the SEM for all samples and standards, illustrating the percentage of the major elements as oxides. On figure 5, the recommended values for BHVO-2 and Rhy-2 are shown to determine the type of rock from which the samples originated (mafic, intermediate, or felsic).

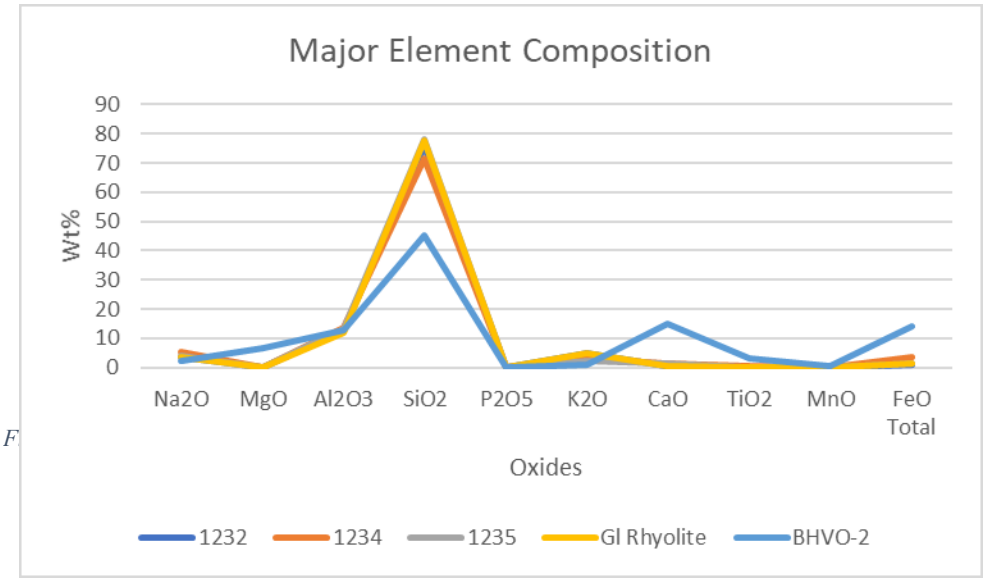

Figure 5. Major element concentrations for all samples and standards.

To identify trace elements present in glass fragments, the samples were analyzed using Laser Ablation Inductive Coupled Plasma-Mass Spectroscopy (LA ICP-MS). The laser is focused on a flat surface of the sample and ablates with a pulsed laser in a gas tight chamber. The ablation produces a stream of particles called aerosols that are transported in a carrier gas to the ICP. Here, the particles are converted to ions, which are then separated by their mass-to-charge ratios using the mass spectrometer. Using a standard for external calibration, the ion signals are converted to the element

concentration. The software utilized to process and convert the data is Glitter 4.4.4, which provides real-time interactive data reduction for LAM-ICPMS analysis. After the data were collected, the standard deviation and/or the mean deviation was calculated for the standards and samples. The standard runs provide proof of the stability of the instrument and determine if there is any instrument drift. By looking at the averages at the beginning of the run, the middle, and the end, any systematic changes in the concentrations could be determined. If the instrument drift is substantial, corrections need to be made. Once the values meet acceptable criteria, the standards are compared to recommended concentrations published by the United States Geological Survey (USGS). Afterwards, a multi-element plot is created illustrating all trace elements from the samples with increasing atomic number on the x axis and their concentration divided by primitive mantle showing on the y axis using a log scale to create a smoother pattern. The pattern created by the plots show characteristics of the primary mantle and determines the samples geologic setting. The trace element data collected is also used to create a variety of x-y plots which facilitate the comparison of glass compositions by illustrating any variations between ashes from each site. Trace elements can be plotted against one another or plotted versus a major element oxide depending on the purpose of the study (Blatt et al., 2006).

Ash Identification

Following the collection of chemical data, the chemical results were compared with each other and with published analyses of volcanic rocks from different data sources. One such source is EarthChem (earthchem.org), which develops and maintains

the database, software, and services that support the preservation, discovery, and analysis of geochemical data, EarthChem also facilitates their integration with the broad array of other available earth science parameters used to compare the ash results to those from explosive volcanic centers in the SVZ and other large eruptive volcanoes worldwide. EarthChem is operated by a team of geoscientists, data scientists, data managers and information technology developers who are part of the NSF-funded data facility Integrated Earth Data Applications (IEDA). Analyses drawn directly from the geological/geochemical literature were also used for comparison. The samples were also compared to volcanic eruptions of the same time period shown on the Global Volcanic Program (GVP) of the Smithsonian Institution National Museum of Natural History and The Large Magnitude Explosive Volcanic Eruptions (LaMEVE) databases. The GVP (volcano.si.edu) documents and disseminates information about volcanic activities through reporting, archiving, researching, and outreach. Collecting data since 1968, the GVP has documentation of current and past volcanic activities for the last 10,000 years. The LaMEVE is a searchable database of the location, age, and magnitude of Quaternary Large Magnitude Explosive Volcanic Eruptions with information on nearly 3,000 volcanoes and over 1,800 Quaternary eruption records.

DATA AND RESULTS

Physical characteristics of samples:

Physical analysis of the samples reveals several differences in their overall appearances. As seen in figure 13a (Appendix A), the ash layer at Site 1232 is made

almost entirely out of glass shards. Minerals present in the sample consist mostly of biotite, quartz, and feldspars, with some fossils (foraminifera) appearing in small quantities. The glass shards possess thin vesicular walls with angular shapes. The ash layer from Site 1233 consists of dark materials with few glass particles. Magnetic minerals are found in large quantities at Site 1233 (figure 13b). The glass shards present in the site 1233 sample are thick and seem to be devitrified. Before wet sieving, samples from sites 1233 and 1234 (figure 13c) looked alike to the eye. Both possessed a brownish to grayish color and were fine grained. After wet sieving the differences became evident. While Site 1234 also has magnetic materials and dark particles, they are found in smaller quantities, compared with Site 1233. There is also a large proportion of glass shards present in sample 1234, with thick walls and better-preserved vesicles than at Site 1232. The edges are also angular. Biotite is present in the sample, as is feldspar. Ash from Site 1235 (figure 13d) shows a large amount of glass with angular shapes and thin walls. Unlike any of the other samples, Site 1235 has a large number of white particles present (devitrifed glass perhaps). No further analysis was done on the minerals present in each site because that was outside the scope of the study.

Major element results:

The semi-quantitative data collected from the SEM provided important information regarding major element composition of the samples. Figure 5 shows all major elements presente in the samples and compares them to the standards BHVO-2 and Rhyolite. The three columns on the right are the recommended values provided by the USGS. Data from SiO_2 collected with the EDS is ploted against trace elements. These oxide vs trace elements tables are an important factor for ash identification.

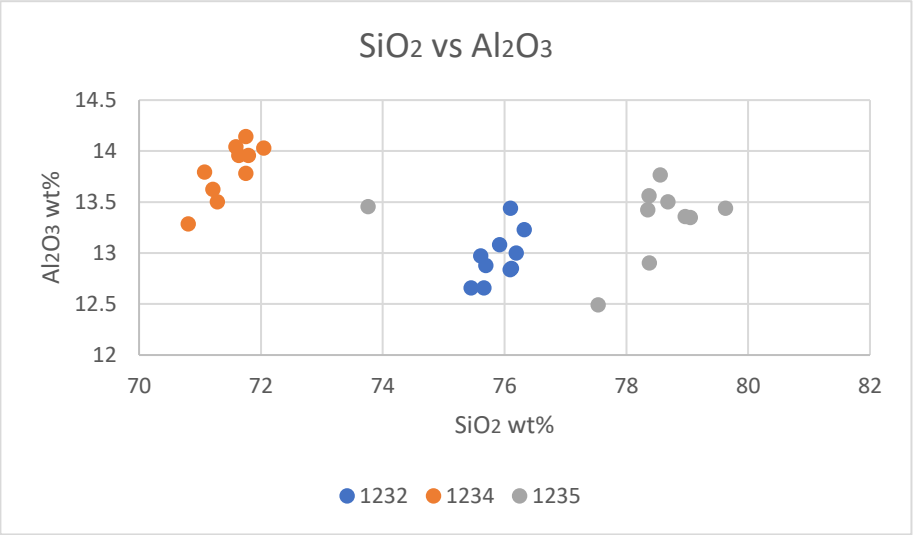

Figure 6a. Major element comparison, SiO2 vs Al2O3.

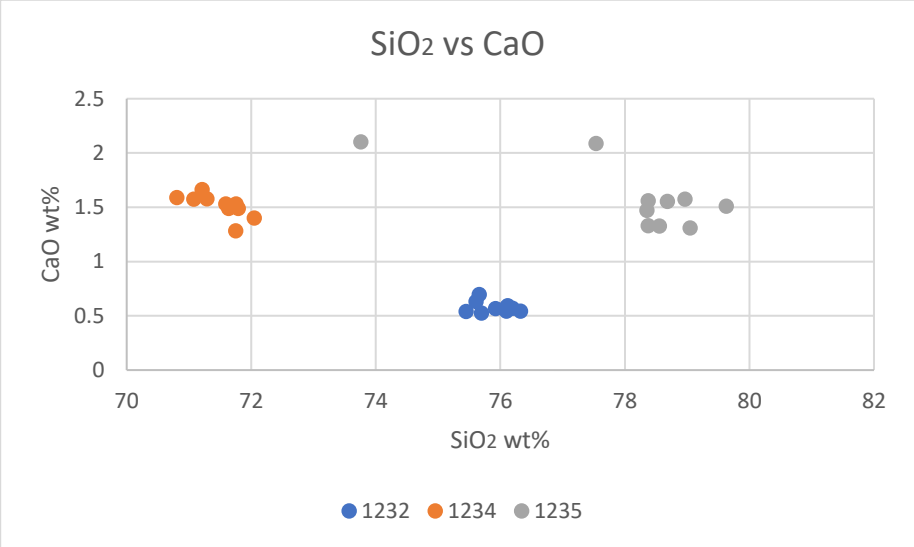

Figure 6b. Major element comparison, SiO2 vs CaO.

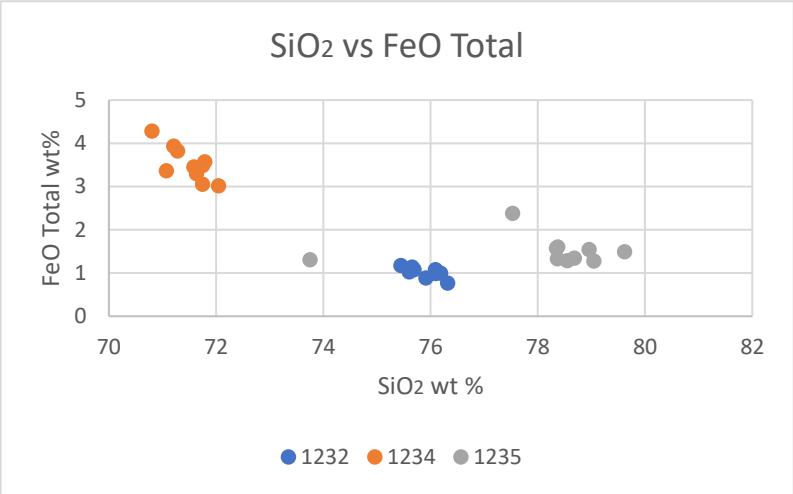

Figure 6c. Major element comparison, SiO2 vs FeO.

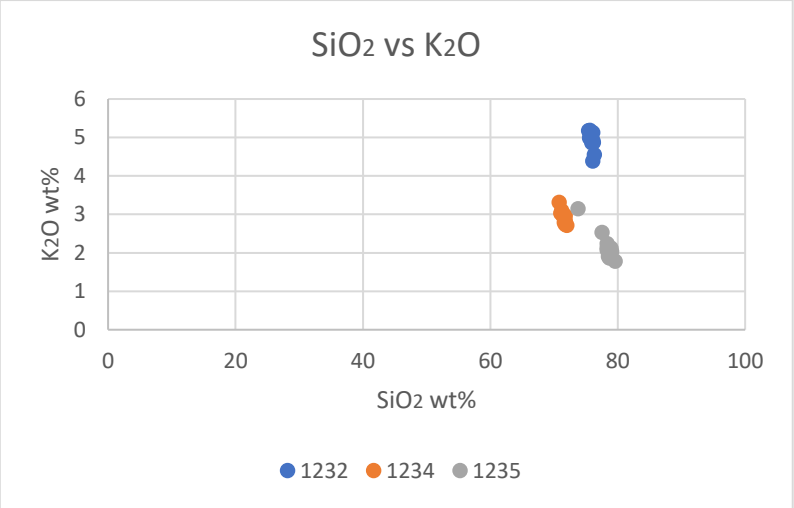

Figure 6d. Major element comparison, SiO2 vs K2O.

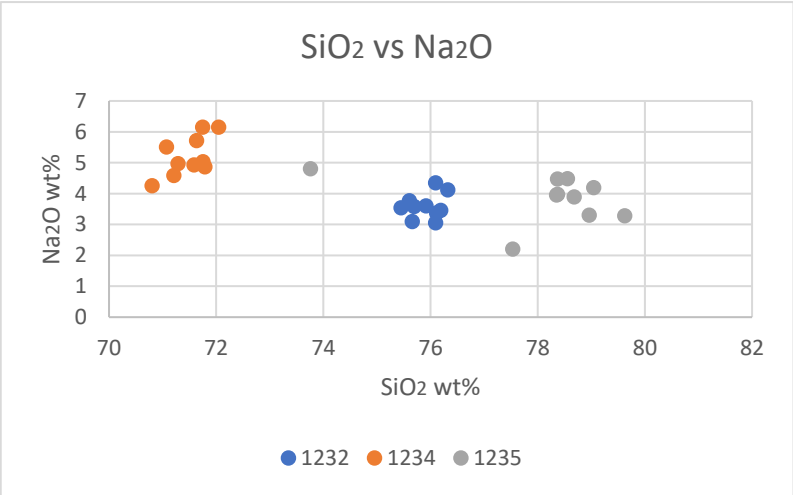

Figure 6e. Major element comparison, SiO2 vs Na2O.

Major elements from Site 1233 (Figure 4) show that the concentration of oxides from aluminum, sodium, and phosphorous are very high in comparison to those from the other sites while silica is very low. Trace element data for ash from Site 1233 showed samples with very low trace element concentrations and others with very high concentrations. Since these properties are not consistent with those of volcanic glass, but are most likely mineral grains, Site 1233 is not shown in the element plots or the multi-element plots. Data for Site 1233 are presented in the Appendix.

Trace element results:

The Spider Diagram

The spider diagrams or multi-element plots show very consistent readings for all sites. The Y axis is shown in log scale for a smoother pattern. All sites show somewhat smilar high and low peaks. Titanium is depleted at all three sites, as well as Strontium and Niobium. Sites 1232 and 1234 have a high Thorium peak, but Site 1232 also has a high Rubidium peak. A small Barium peak is seen in Site 1235.

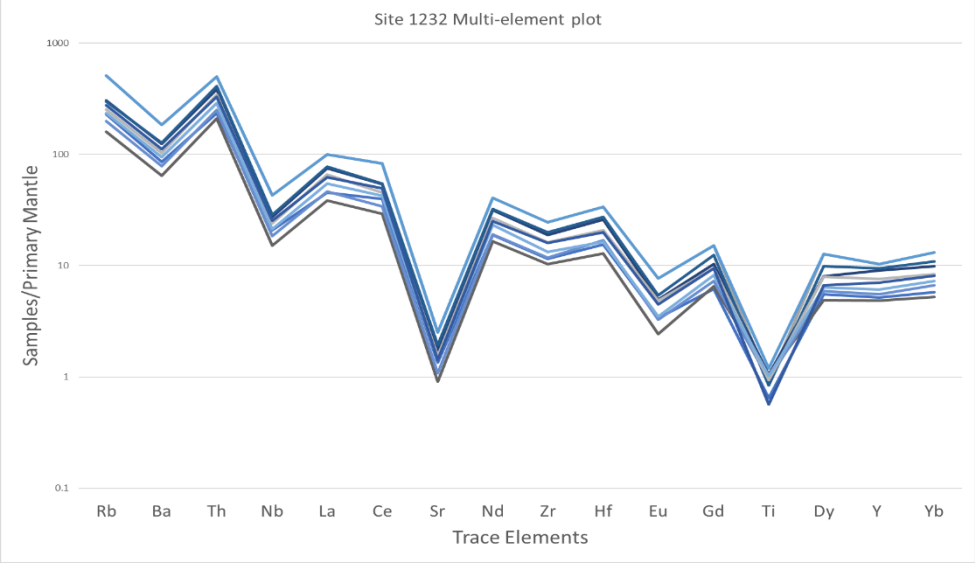

Figure 7a. Multi-element plot for Site 1232. Each line represents the data collected for a glass shard.

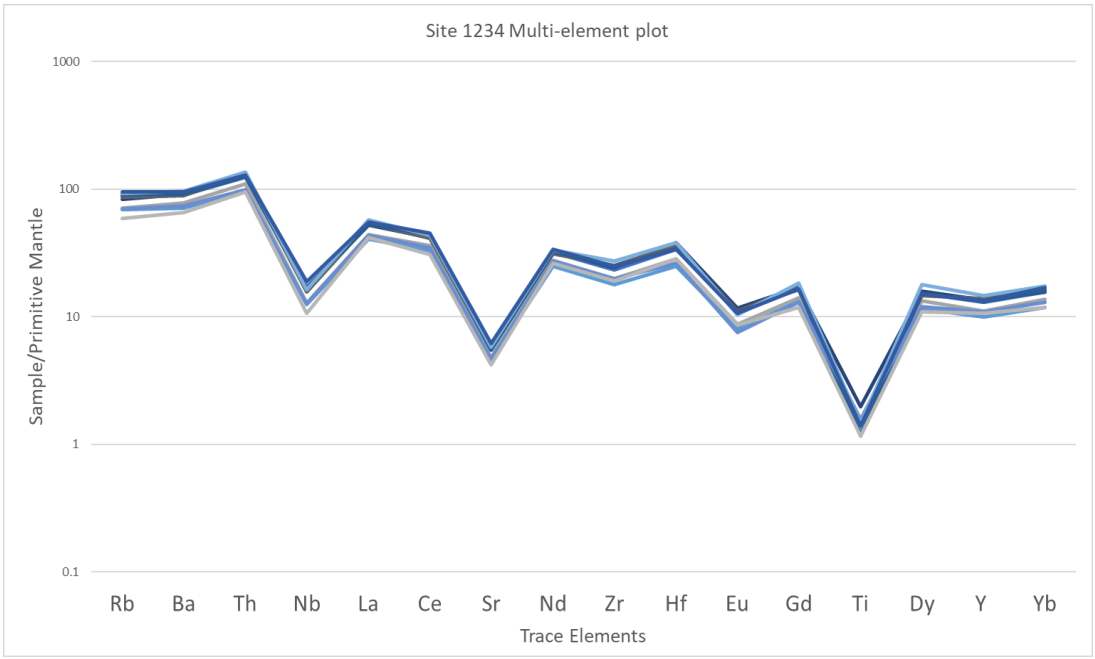

Figure 7b. Multi-element plot for Site 1234. Each line represents the data collected for a glass shard.

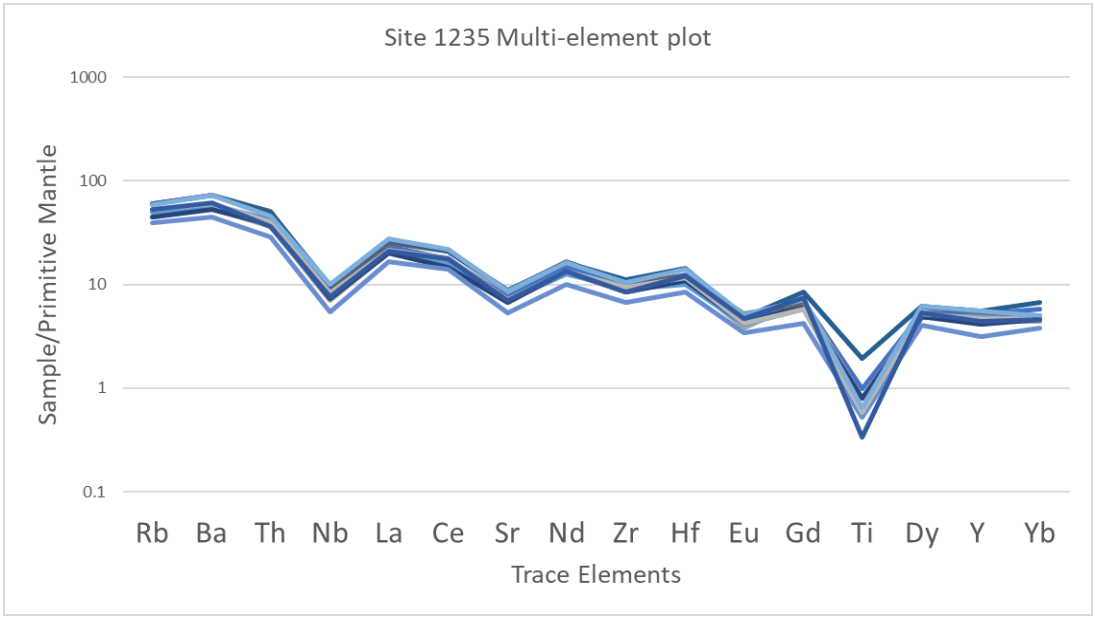

Figure 7c. Multi-element plot for Site 1235. Each line represents the data collected for a glass shard.

Trace Element Bivariate Plots

Figure 8. X vs Y plots for trace elements.

Lastly, chemical analysis of selected trace elements plotted against SiO_2.

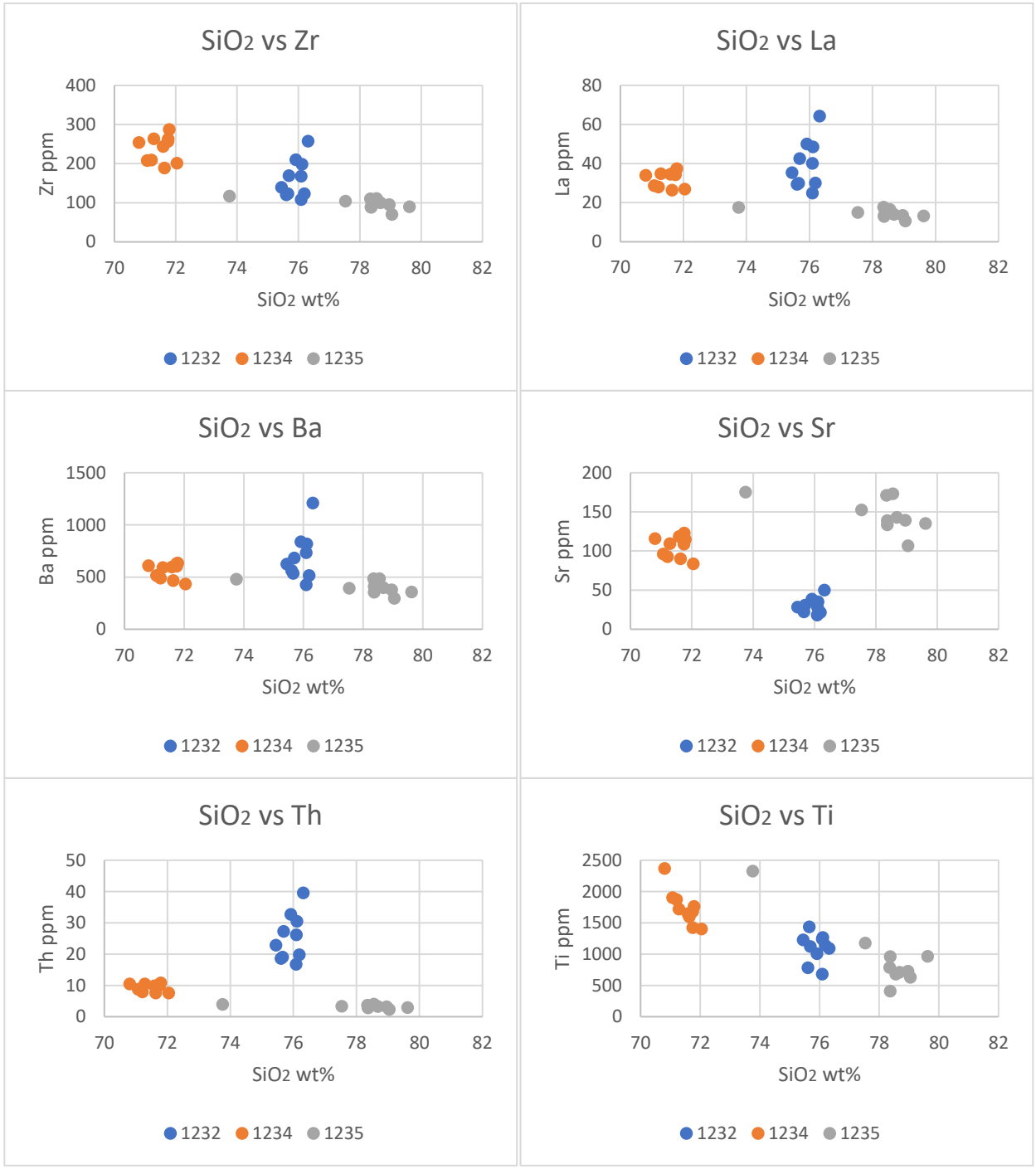

Figure 9. SiO2 vs Trace Elements.

Interpretations derived from the physical characteristics of samples

Physical observations of samples from all sites reveal differences among them. Samples from sites 1233 and 1234 possessed darker tones even before wet sieving, in contrast with the lighter tones of sites 1232 and 1235. Because of the darker tones, and the fact that samples from sites 1233 and 1234 were collected at similar shallow depths, the possibility of the selected glasses having the same volcanic origin seemed possible. However, after closer observation under the light microscope (Figures 10b and 10c), their differences became evident. While glass shards in Site 1234 were easily located, Site 1233 was mainly composed of devitrified glass and feldspars. Because devitrified volcanic glass is harder to identify using chemistry, no further analysis was performed on samples from Site 1233. To be thorough, another sample from Site 1233, in the same core and section, but at different intervals (69.5-70 instead of the original 76-77) was collected and prepared using the same techniques yielding similar results. Devitrified glass shards with highly magnetic mineral were consistently present in the 1233 sample.

Physical traits to consider for glass morphology analysis are shape and vesicularity (Scasso and Carey, 2005). The shape of the glass shards shows the conditions in which they were deposited (Scasso and Carey, 2005). The geometry shown in shards is a result of transportation after deposition, which in turn explains any changes in the chemical composition associated with weathering. Post-depositional weathering can result in crystallization in the glass shards, a process called devitrification. Backscattered images produced using the SEM show that all samples except from Site 1233 are highly

angular with little to no rounded edges, which is a trait observed in undisturbed sediments. The angular shapes lead to the conclusion that the samples traveled by wind from their place of origin towards the Pacific coast of Chile and descended to the ocean floor, without being transported from land by water. Latter methods of transportation would produce abrasion which could be detected by simple physical observations. The glass shards were for the most part colorless and transparent, only samples from Site 1233 possessed traces of coloration (yellowish). Transparent glass shards are obtained by little to no alteration by seawater. These characteristics are consistent with the particles being ash, transported in the atmosphere and deposited from the air and settling through the ocean water column. The vesicular properties of the ash samples provide the other half of the story. Vesicles are the empty cavities on glass shards produced by gas bubbles. As the bubbles grow, magmatic viscosity increases exponentially due to the loss of water in the form of gas and other volatile components, a process caused by diffusion during magma ascent (Scasso and Carey, 2005). Magmas with higher SiO_2 content tend to be more viscous and have a higher dissolved gas content. This means that the number of vesicles, and their size shows the magmatic origins, and by doing so, the eruption type. The glass shards from all sites contained vesicles at some point, illustrated by the patterns of fragmentation. A great example of this can be seen in glass shards from Site 1235 (Figure 11d). In figures 11d E and F, the path of fragmentation is shown to be caused by the ruptures of the walls of the gas filled vesicles. On the basis of these physical observations, it can be inferred that the ash samples possess high concentrations of SiO_2, and that they originated from viscous, gas-rich magmas which produce explosive eruptions.

Interpretations derived from the major element composition of the samples

These observations are backed up by the major element analyses of individual glass shards. The chemical composition on all shards from sites 1232, 1234, and 1235 show a consistent rhyolitic composition (SiO_2 for Site 1232= 75.88 ± 0.44 wt%, Site 1234= 71.42± 0.62 wt%, and Site 1235= 76.68± 2.93 wt%). Plotting the samples on a Harker diagram reveals some clear distinctions between samples from all sites. Figure 10 shows samples from Site 1232 being between alkaline and high calc-alkaline. While samples from sites 1234 and 1235 range from high-K calc-alkaline and calc-alkaline, with samples from Site 1235 being less K rich than samples from Site 1234. For Site 1232, the oxides vs SiO_2 diagrams show a general decrease in CaO and FeO total, with increasing SiO_2. Site 1234 has the highest weight percentage of FeO total which correlates with a lower content of SiO_2. This shows that, as silica content increases, mafic minerals, especially Fe-Ti oxides, are differentiated out of the magma. Al_2O_3 is fairly constant in all samples, as is CaO and Na_2O.

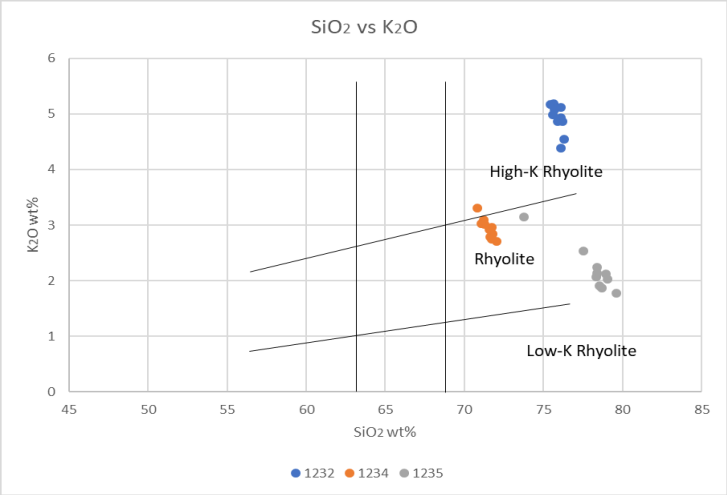

Figure 10. The SiO2 vs K2O Diagram for sites 1232, 1234, and 1234.

Interpretations based on trace element patterns in the samples

The major element analysis shows that all samples belong to regions with arc magmatism with late-stage fractionation. However, major elements cannot distinguish between continental magmatic arcs and island arcs (Blatt et al., 2006), or between different explosive eruptions. Trace elements on the other hand, can reveal much more about the diverse origins and evolution of magmatic arc rocks. Trace elements will either substitute for a major element inside the crystal structure of the mineral or remain in the liquid phase (Blatt et al., 2006). During magmatic differentiation, some elements are excluded from the minerals that form (incompatible elements), while others are incorporated into the mineral structure (compatible elements). Incompatible elements can be divided into several groups: the large-ion lithophile elements (LILE, K, Rb, Ba), high-field strength elements (HFSE, Nb, Zr, Hf, Th), and rare earth elements (La, Sm, Eu, Gd, Yb and Y). These elements can be plotted on a graph to show enrichment or depletion of trace elements compared with each other. Elemental abundances are normalized to a standard set of values, such as "primitive mantle" (McDonough and Sun 1989) for comparison and plotted from left to right in order of increasing compatibility during mantle melting. Trace element analysis of the ash samples shows features predominant in magmas from active continental margins and subduction zones generally, such as depletion of Nb in all 30 samples, enrichment of LILE compared with light rare earth elements (LREE) (Kilian and Behrmann, 2003). Sr plots below other elements, indicating the differentiation of feldspar in the magmas. Titanium is also depleted in all samples which is a common trait in silic rich magmas resulting from crystallization of Fe-Ti oxides. Overall, the primitive mantle-normalized patterns display enriched LREE

relative to the heavy rare earth elements (HREE), which can be an original feature of primitive magmas or a sign of interaction between the magma with the crust. An important point is that the average normalized trace element patterns of the different sites have some characteristics that are distinct. For example, for all sites highly incompatible elements Rb, Ba and Th have different relative abundances, and enrichment of LREE relative to HREE is greater at Site 1232 compared with sites 1234 and 1235.

Plots of incompatible elements versus each other show linear trends with concentrations of elements within glass shards from the three sites varying by factors of 1.5 – 2. These trends converge on zero, which indicates constant ratios of the elements compared with each other. Some of the variation of incompatible element concentrations in the glass shards is probably related to magmatic differentiation, although SiO_2 does not vary much at the high rhyolitic values. The variation may reflect the dilution of the elemental signal during laser analysis by minute feldspar and quartz crystals and open space in vesicles. None of the three sites have exactly the same incompatible element ratios as another. For example, Sr is higher relative to Y in Site 1235 ash. La is high relative to REE Gd and Yb at Site 1232, confirming LREE-enrichment. Ba/Th, and Th/La are also higher at Site 1232, while Zr/Nb is lower. These differences can be used to distinguish ash from the different sites and potentially to identify their volcanic source.

DISCUSSION

Based on comparisons of major and incompatible element patterns in Figure 9, it is clear that none of the three ash layers were deposited from exactly the same volcanic source. Therefore, the studied ash layers in the selected Leg 202 sediments cannot be correlated or used as a time horizon.

In order to attempt to identify potential volcanic sources, I compared the ash patterns to those of some known SVZ volcanic sources. The lists of Pleistocene and recent explosive eruptions collected from the LaMEVE and the Smithsonian databases provides a useful starting point from which to determine the origin of the samples. A more specific eruption database for the SVZ compiled by Fontjin et al. (2014) was filtered to provide SVZ eruptive centers having: 1) VEI > 5, 2) Pleistocene to Recent age, and 3) rhyodacite and rhyolitic products. This yielded 3 centers: Quizapu (escabezados Grande/Cerro Azul); Puyehue Cordon-Caulle and Chaiten Volcano. Chemical data were extracted for rhyolites from these locations using the EarthChem database, as well as literature sources. These comparisons are shown in figure 11a, b, and c.

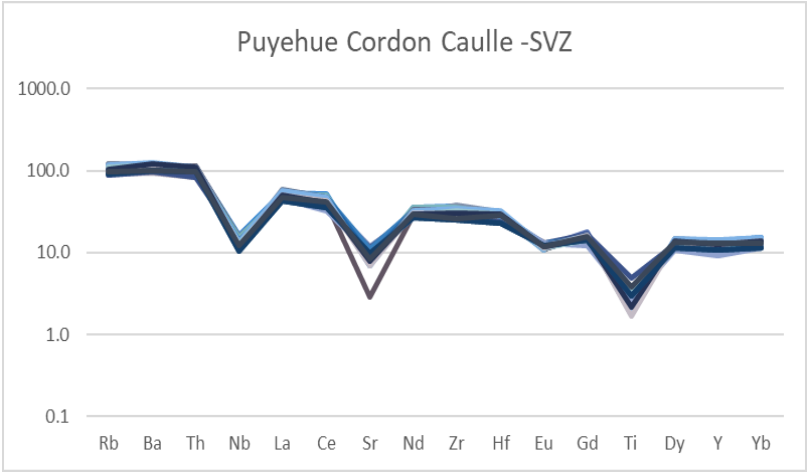

Figure 11a. Multi-element plot of Puyehue Cordon-Caulle.

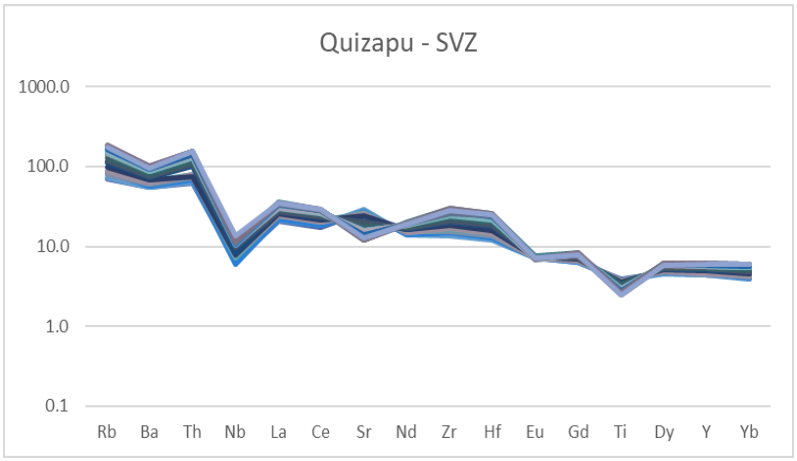

Figure 11b. Multi-element plot of Quizapu.

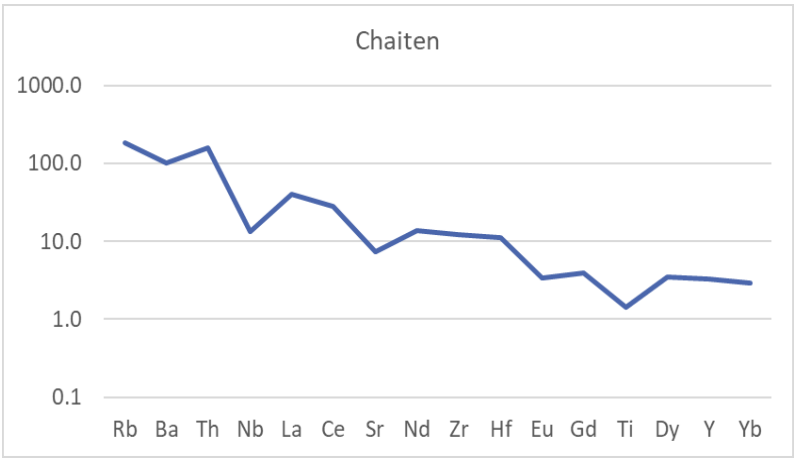

Figure 11c. Multi-element plot of Chaiten.

Comparing the selected data to the samples yields some interesting results (Figure 15, Appendix C). Site 1232 resembles the multiplot for the Chaiten volcano except for the negative Sr and Ti values in 1232, which are much more depleted (>1) than those in Chaiten. Depletion of Ti is a common trait in all sites, with some degrees of variation in Site 1235, a trait seen in Puyehue Cordon-Caulle as well. Although overall values for Site 1235 are a bit lower than those in Puyehue Cordon-Caulle, their patterns

are very similar. From the late Pleistocene, Cordon Caulle emitted only rhyodacites and rhyolites (Lara et al., 2006) which makes it a viable location for Site 1232's origins. Site 1234 and Chaiten share some similarities as well, with the LILE (except for Rb), and Th, Nb, La, Ce, and Sr plotting similar results. However, the rest of the elements are not compatible.

In addition, data were compared with the Okataina volcanic complex in the Taupo Volcanic Zone, NZ, at latitiude 38°S, which has produced numerous eruptions with VEI >5 during the Pleistocene/Recent. This comparison is shown in Figure 12, where depletion of Nb, Sr, and Ti resembles that of Site 1234. And unlike Chaiten, the results are consistent.

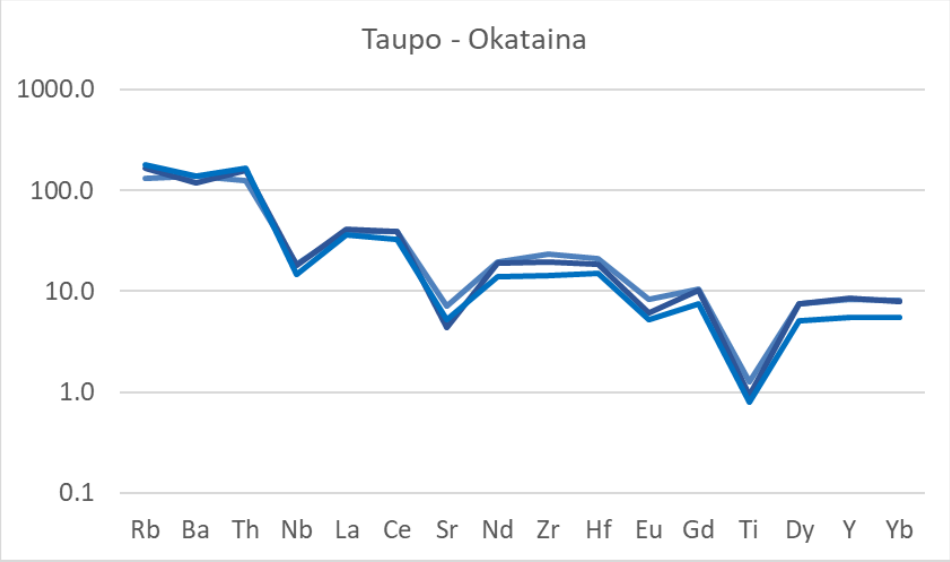

Figure 12. Multi-element plot of Taupo-Okataina.

Conclusions

Analysis for all samples were based upon physical and chemical interpretations. Information gathered in this project indicate that the ashes have distinct geochemical signatures which could be matched to specific eruptions. However, it is impossible to accurately determine the source(s) at this time without a more thorough compilation of a database for comparison. The compilation of tephra records for Chile shows a vast majority of insufficiently characterized layers to allow for the sources to be properly identified (K. Fontijn et al., 2014). Even the most widely used method of tephra identification, major element analysis of individual glass shards, has some particular complications in southern Chile. Take for example the two most recent explosive eruptions in the area, the 2008 rhyolitic eruption in Chaiten, and the 2011 rhyodacite in Puyehue Cordon-Caulle. The chemical composition of major elements was almost indistinguishable from the previous eruptions at the same volcanoes (K. Fontijn et al., 2014). Taking this into consideration, the one definitive conclusion is that the same explosive eruption did not produce the three ash layers.

Future directions

Additional research such as analysis of radiogenic isotopes could prove useful as an additional parameter for narrowing the gap between the known and the unknown. The study of selected minerals such as biotite present in Site 1232 and 1234, and Site 1235 in smaller quantities, could be used as geochronological indicators. Microfossils such as foraminifera, found at Site 1232, might also be used to determine the age of the samples, making it easier to locate its origin.

REFERENCES

Anonymous. (2007). Ocean Drilling Program final technical report, 1983-2007 . College Station, TX: Texas A&M University, Ocean Drilling Program, College Station, TX, United States. http://www-odp.tamu.edu/publications/ODP_Final_Technical_Report.pdf

Baines, P. G., & Sparks, R. S. J. (2005). Dynamics of giant volcanic ash clouds from supervolcanic eruptions. *Geophysical Research Letters*, *32*(24).

Bard, Edouard & Arnold, Maurice & Mangerud, Jan & Paterne, Martine & Labeyrie, Laurent & Duprat, Josette & Mélières, Marie-Antoinette & Sønstegaard, Eivind & Duplessy, Jean-Claude. (1994). The North Atlantic atmosphere-sea surface 14C gradient during the Younger Dryas climatic event. Earth and Planetary Science Letters. 126. 275-287. 10.1016/0012-821X(94)90112-0.

Blatt, H., Tracy, R. J., & Owens, B. E. (2006). Petrology: Igneous, sedimentary, and metamorphic. New York: W.H. Freeman.

Carel, Mélanie, Giuseppe Siani, and Guillaume Delpech. "Tephrostratigraphy of a Deep-Sea Sediment Sequence Off the South Chilean Margin: New Insight into the Hudson Volcanic Activity since the Last Glacial Period." Journal of Volcanology and Geothermal Research 208.3 (2011): 99-111. Web.

Crosweller, H. S., Arora, B., Brown, S. K., Cottrell, E., Deligne, N. I., Guerrero, N. O., ... & Nayembil, M. (2012). Global database on large magnitude explosive volcanic eruptions (LaMEVE). Journal of Applied Volcanology, 1(1), 4.

Feininger, T. (2001). An Introduction to Igneous and Metamorphic Petrology. By John D. Winter. Prentice-Hall Inc.(available in Canada from Pearson Education Canada, 195 Harry Walker Parkway North, Newmarket, Ontario L3Y 7B4.) xx+ 697 pages, CDN $107.48, ISBN 0-13-240342-0. *The Canadian Mineralogist*, *39*(5), 1503-1505.

Fontijn, K., Lachowycz, S. M., Rawson, H., Pyle, D. M., Mather, T. A., Naranjo, J. A., & Moreno-Roa, H. (2014). Late Quaternary tephrostratigraphy of southern Chile and Argentina. *Quaternary Science Reviews*, *89*, 70-84.

Goldstein, J. I., Newbury, D. E., Echlin, P., Joy, D. C., Lyman, C. E., Lifshin, E., ... & Michael, J. R. (2003). Special Topics in Scanning Electron Microscopy. In Scanning Electron Microscopy and X-Ray Microanalysis (pp. 195-270). Springer US.

Geochemical constraints on the sources of Southern Chile Trench sediments and their recycling in arc magmas of the Southern Andes ROLF KILIAN1 & JAN H. BEHRMANN 2003

Gerlach, D.C., Frey, F.A., Moreno-Roa, H., Lopez-Escobar, L., 1988. Recent volcanism in the Puyehue-Cordon Caulle region, Southern Andes (40.5oS): Petrogenesis of evolved lavas. Journal of Petrology 29, 333-382.

Hickey-Vargas, Rosemary, et al. "Basaltic Rocks from the Andean Southern Volcanic Zone: Insights from the Comparison of Along-Strike and Small-Scale Geochemical Variations and their Sources." LITHOS 258-259 (2016a): 115-32. CrossRef. Web.

Hickey-Vargas, R., M. Sun, and S. Holbik. "Geochemistry of Basalts from Small Eruptive Centers Near Villarrica Stratovolcano, Chile: Evidence for Lithospheric Mantle Components in Continental Arc Magmas." Geochimica et Cosmochimica Acta 185 (2016b): 358-82. CrossRef. Web.

Hickey -Vargas, Rosemary, et al. "Geochemical Variations in Andean Basaltic and Silicic Lavas from the Villarrica-Lanin Volcanic Chain (39.5 S): An Evaluation of Source Heterogeneity, Fractional Crystallization and Crustal Assimilation." Contributions to Mineralogy and Petrology 103.3 (1989): 361-86. CrossRef. Web.

Hong, Wentao & Xu, Xisheng & Zou, Haibo. (2013). Petrogenesis of coexisting high-silica aluminous and peralkaline rhyolites from Yunshan (Yongtai), southeastern China. Journal of Asian Earth Sciences. 74. 316-329. 10.1016/j.jseaes.2013.01.005.

Jicha, B.R., Singer, B.S., Beard, B.L., Johnson, C.M., Moreno-Roa, H., Naranjo, J.A., 2007. Rapid magma ascent and generation of (super 230) Th excesses in the lower crust at Puyehue-Cordon Caulle, Southern Volcanic Zone, Chile. Earth and Planetary Science Letters 255, 229-242.

JOIDES resolution fact sheet https://iodp.tamu.edu/labs/ship/ship_brochure.pdf

Keller, J., Ryan, W. B. F., Ninkovich, D., & Altherr, R. (1978). Explosive volcanic activity in the mediterranean over the past 200,000 yr as recorded in deep-sea sediments. Geological Society of America Bulletin, 89(4), 591-604. Retrieved from http://ezproxy.fiu.edu/login?url=https://search-proquest-com.ezproxy.fiu.edu/docview/52136361?accountid=10901

Lara, L.E., Moreno, H., Naranjo, J.A., Matthews, S., Perez de Arce, C., 2006a. Magmatic evolution of the Puyehue-Cordon Caulle volcanic complex (40 degrees S), Southern Andean Volcanic Zone; from shield to unusual rhyolitic fissure volcanism. Journal of Volcanology and Geothermal Research 157, 343-366.

Liu, E. J., Cashman, K. V., Rust, A. C., & Gislason, S. R. (2015). The role of bubbles in generating fine ash during hydromagmatic eruptions. Geology (Boulder), 43(3), 239-242. doi:http://dx.doi.org.ezproxy.fiu.edu/10.1130/G36336.1

Lopez-Escobar, L., Kilian, R., Kempton, P.D., Tagiri, M., 1993. Petrography and geochemistry of Quaternary rocks from the Southern Volcanic Zone of the Andes between 41 degrees 30' and 46 degrees 00'S, Chile. Revista Geologica de Chile 20, 33-55.

Lyubetskaya, T., & Korenaga, J. (2007). Chemical composition of earth's primitive mantle and its variance; 1, method and results. Journal of Geophysical Research, 112, B03211. doi:http://dx.doi.org.ezproxy.fiu.edu/10.1029/2005JB004223

McDonough, W. F., & Sun, S. S. (1995). The composition of the earth. Chemical Geology, 120(3-4), 223-253. doi:http://dx.doi.org.ezproxy.fiu.edu/10.1016/0009-2541(94)00140-4

McIlroy, Duncan. "T. Moreno & W. Gibbons (Eds) 2007. the Geology of Chile. Viii + 414 Pp. London, Bath: Geological Society of London. Price £85.00 (Hard Covers), £35.00 (Paperback). ISBN 9781 86239 219 9; 9781 86239 220 5 (Pb)." Geological Magazine 146.1 (2009): 156. CrossRef. Web.

Mix, A. C., Tiedemann, R., Blum, P., Abrantes, F. F., Benway, H., Cacho-Lascorz, I., . . . Wei, W. (2003a). Leg 202 summary. Proceedings of the Ocean Drilling Program, Part A: Initial Reports, 202, 145. doi:http://dx.doi.org.ezproxy.fiu.edu/10.2973/odp.proc.ir.202.101.2003

Mix, A. C., Tiedemann, R., Blum, P., Abrantes, F. F., Benway, H., Cacho-Lascorz, I., . . . Wei, W. (2003b). Proceedings of the ocean drilling program, initial reports, southeast pacific paleoceanographic transects; covering leg 202 of the cruises of the drilling vessel JOIDES resolution; valparaiso, chile, to balboa, panama; sites 1232-1242, 29 march-30 may 2002. Proceedings of the Ocean Drilling Program, Part A: Initial Reports, 202, variously paginated. doi:http://dx.doi.org.ezproxy.fiu.edu/10.2973/odp.proc.ir.202.2003

Moreno, T. & Gibbons, W. (eds) 2007 The Geology of Chile. The Geological Society, London.

Murray, J. J. (2015). The US Interagency Volcanic Hazards Sciences and Services Coordination Group.

Niemeier, U., Timmreck, C., Graf, H. F., Kinne, S., Rast, S., & Self, S. (2009). Initial fate of fine ash and sulfur from large volcanic eruptions. Atmospheric Chemistry and Physics, 9(22), 9043-9057. Retrieved from http://ezproxy.fiu.edu/login?url=https://search-proquest-com.ezproxy.fiu.edu/docview/886914393?accountid=10901

Reid, Mary. R., and Jorge. A. Vazquez (2017) Fitful and protracted magma assembly leading to a giant eruption, Youngest Toba Tuff, Indonesia, Geochem. Geophys. Geosyst., 18, 156–177, doi:10.1002/2016GC006641.

Robinson, Frank A., (2016) Variation in rhyolitic magma composition linked with fractionation from a common source: insights from the Rotoiti eruption, Taupo Volcanic Zone, New Zealand, International Geology Review 58, 1967-1982, https://doi.org/10.1080/00206814.2016.1196400

Rollinson, H. (1994). Using Geochemical Data: Evaluation, Presentation, Interpretation. J. Wiley and Sons.

Roth, M., and R. Guritz. "Visualization of Volcanic Ash Clouds." IEEE Computer Graphics and Applications (1995): 34-9. Print.

Ruprecht, P., 2012. The crustal magma storage sytem of volcan Quizapu, Chile, and the effects of magma mixing on magma diversity. Journal of Petrology 53, 801-840.

Scasso, R. A., & Carey, S. (2005). Morphology and formation of glassy volcanic ash from the August 12-15, 1991 eruption of Hudson Volcano, Chile. Latin American journal of sedimentology and basin analysis, 12(1), 3-21.

Shang, Cosmas & Satir, Muharrem & Nsifa, Emmanuel & Liégeois, J.-P & Siebel, Wolfgang & Taubald, H. (2007). Archaean high-K granitoids produced by remelting of earlier Tonalite–Trondhjemite–Granodiorite (TTG) in the Sangmelima region of the Ntem complex of the Congo craton, southern Cameroon. International Journal of Earth Sciences. 96. 817-841. 10.1007/s00531-006-0141-3.

Sun, S. (1982). Chemical composition and origin of the earth's primitive mantle. Geochimica Et Cosmochimica Acta, 46(2), 179-192. doi:http://dx.doi.org.ezproxy.fiu.edu/10.1016/0016-7037(82)90245-9

Sun, S. S., & McDonough, W. F. (1989). Chemical and isotopic systematics of oceanic basalts; implications for mantle composition and processes. Geological Society Special

Prata, A. J., Carn, S. A., Stohl, A., & Kerkmann, J. (2007). Long range transport and fate of a stratospheric volcanic cloud from Soufriere Hills volcano, Montserrat. *Atmospheric Chemistry and Physics*, *7*(19), 5093-5103.

Publications, 42, 313-345. Retrieved from http://ezproxy.fiu.edu/login?url=https://search-proquest-com.ezproxy.fiu.edu/docview/50586346?accountid=10901

Turney, C. S. M., Lowe, J. J., Davies, S. M., Hall, V., Lowe, D. J., Wastegard, S., . . . Alloway, B. (2004). Tephrochronology of last termination sequences in europe; a protocol for improved analytical precision and robust correlation procedures (a joint SCOTAV-INTIMATE proposal). JQS.Journal of Quaternary Science, 19(2), 111-120. doi:http://dx.doi.org.ezproxy.fiu.edu/10.1002/jqs.822

Turner, D. L., Triplehorn, D. M., Naeser, C. W., & Wolfe, J. A. (1980). Radiometric dating of ash partings in alaskan coal beds and upper tertiary paleobotanical stages. Geology (Boulder), 8(2), 92-96. Retrieved from http://ezproxy.fiu.edu/login?url=https://search-proquest-com.ezproxy.fiu.edu/docview/51966079?accountid=10901

Venzke, Edward, et al. "Reports from the Smithsonian's Global Volcanism Network, June 2010." Bulletin of Volcanology 73.1 (2011): 113-4. CrossRef. Web.

Venzke, E., Wunderman, R. W., McClelland, L., Simkin, T., Luhr, J. F., Siebert, L., ... & Sennert, S. (2002). Global volcanism, 1968 to the present. Smithsonian Institution, Global Volcanism Program Digital Information Series, GVP-4.

Walker, J. D., Lehnert, K. A., Hofmann, A. W., Sarbas, B., & Carlson, R. W. (2005, December). EarthChem: International collaboration for solid earth geochemistry in geoinformatics. In AGU Fall Meeting Abstracts.

Wilson, S.A., 1997, Data compilation for USGS reference material BHVO-2 Hawaiian Basalt: U.S. Geological Survey Open-File Report

Yanagi, T. (2011). Arc Volcano of Japan: Generation of Continental Crust from the Mantle (Vol. 136). Springer.

APPENDICES

APPENDIX A

Sample images taken using a digital camera from an Optical Microscope.

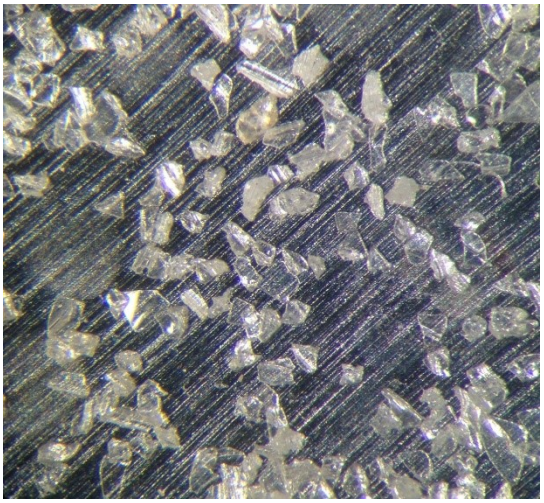

Figure 13a. Digital image from Site 1232.

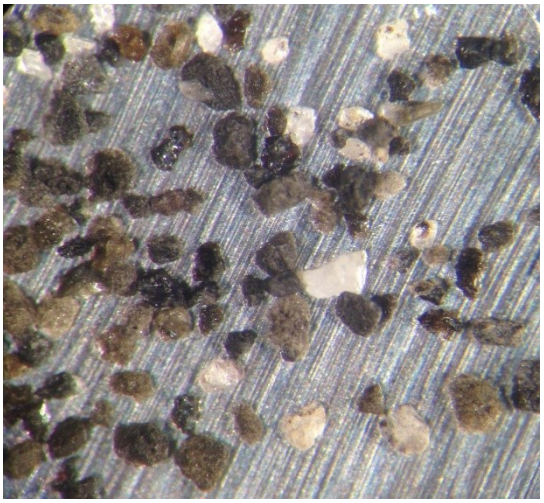

Figure 13b. Digital image from Site 1233.

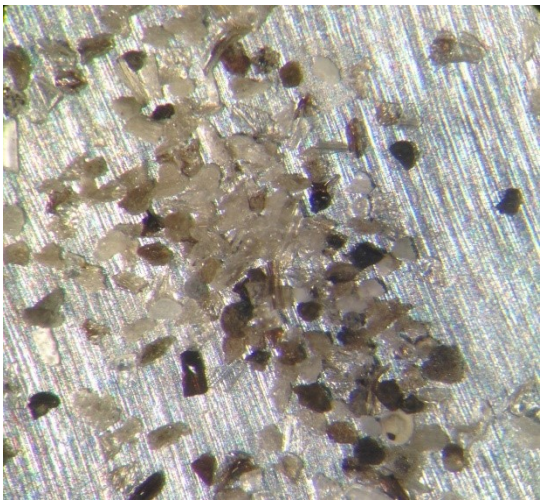

Figure 13c. Digital image from Site 1234.

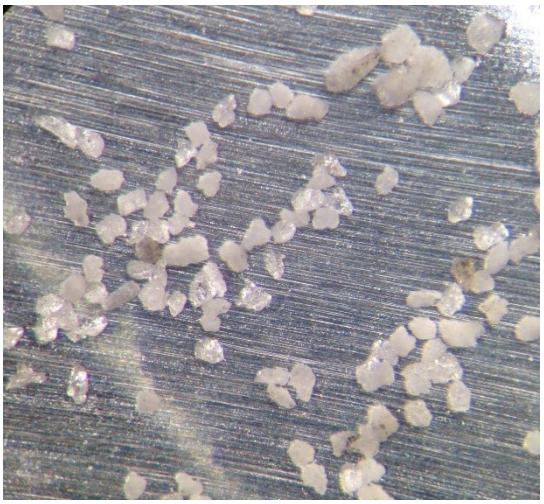

Figure 13d. Digital image from Site 1235.

APPENDIX B

Images from all sites taken with the SEM with 25 kV.

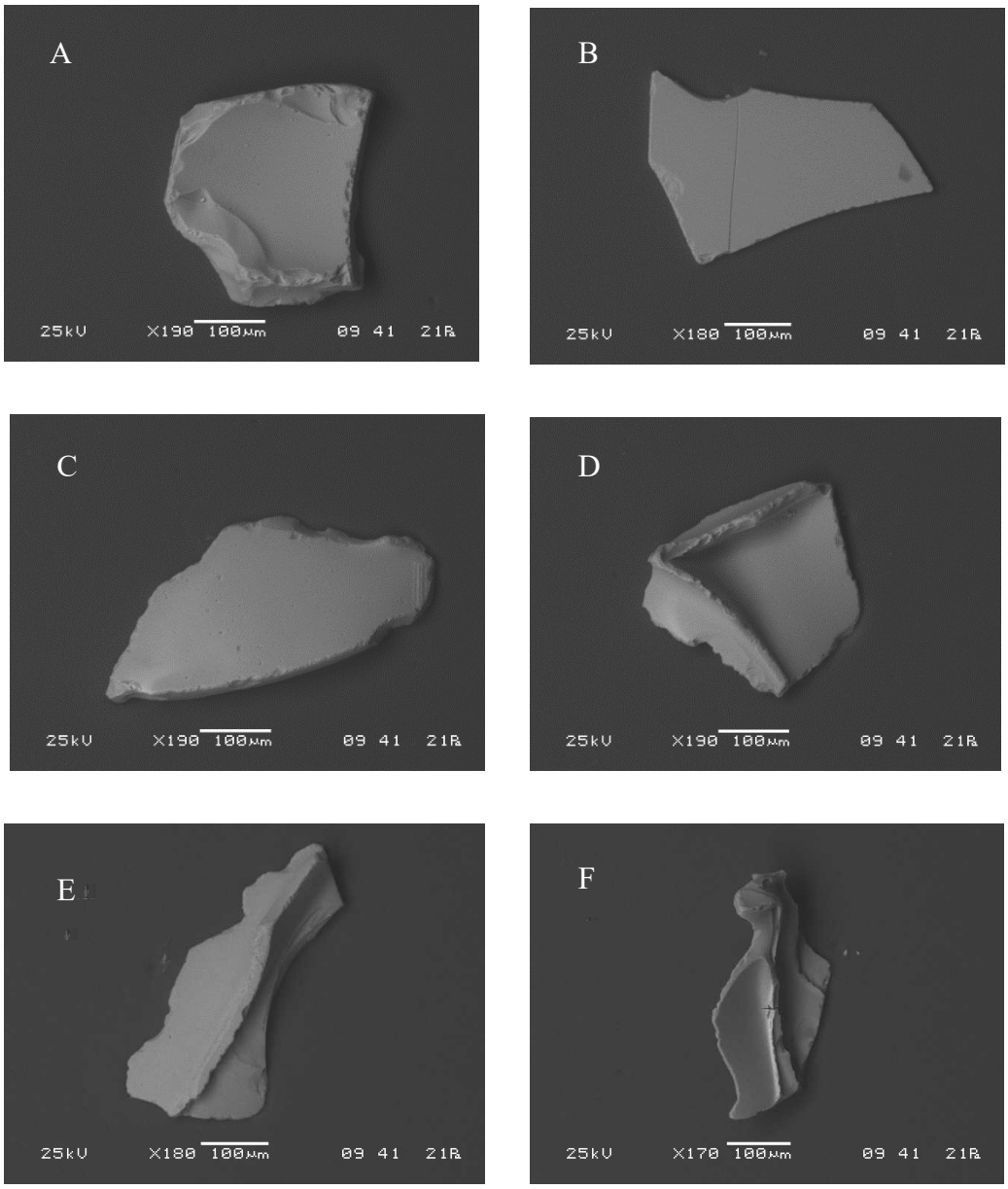

Figure 14a. Glass images taken with the Scanning Electron Microscope for Site 1232.

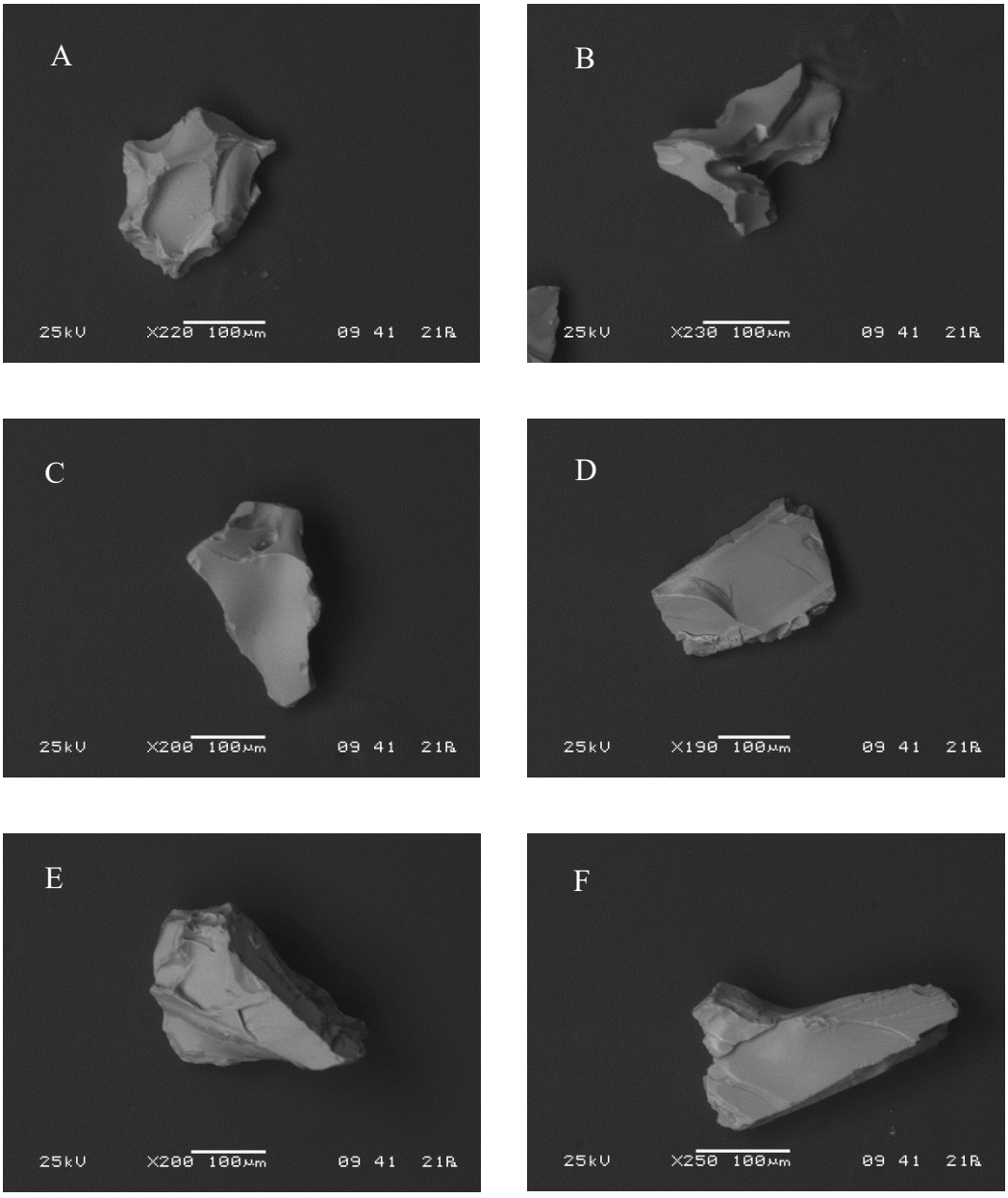

Figure 14b. Glass images taken with the Scanning Electron Microscope for Site 1233.

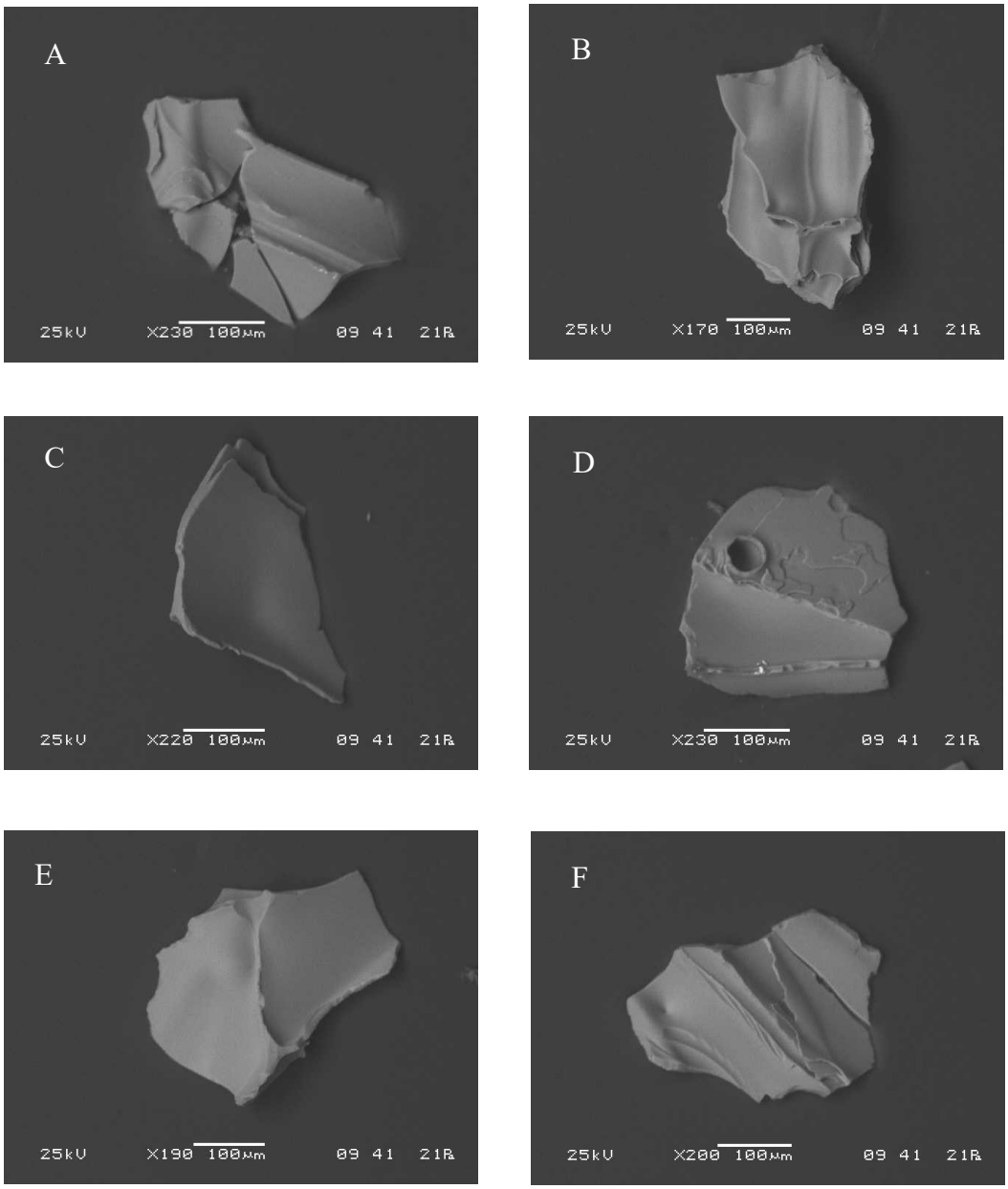

Figure 14c. Glass images taken with the Scanning Electron Microscope for Site 1234.

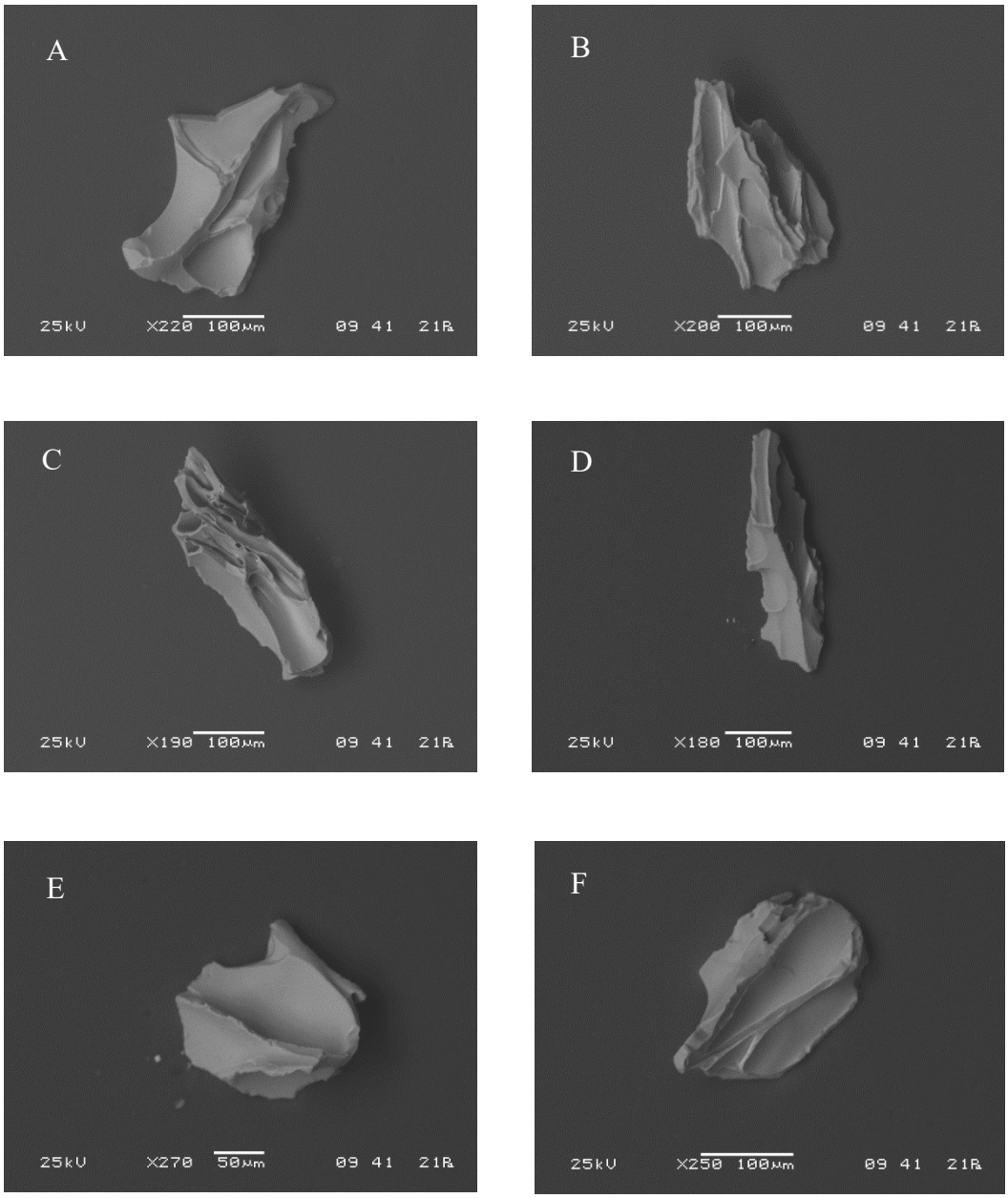

Figure 14d. Glass images taken with the Scanning Electron Microscope for Site 1235.

APPENDIX C

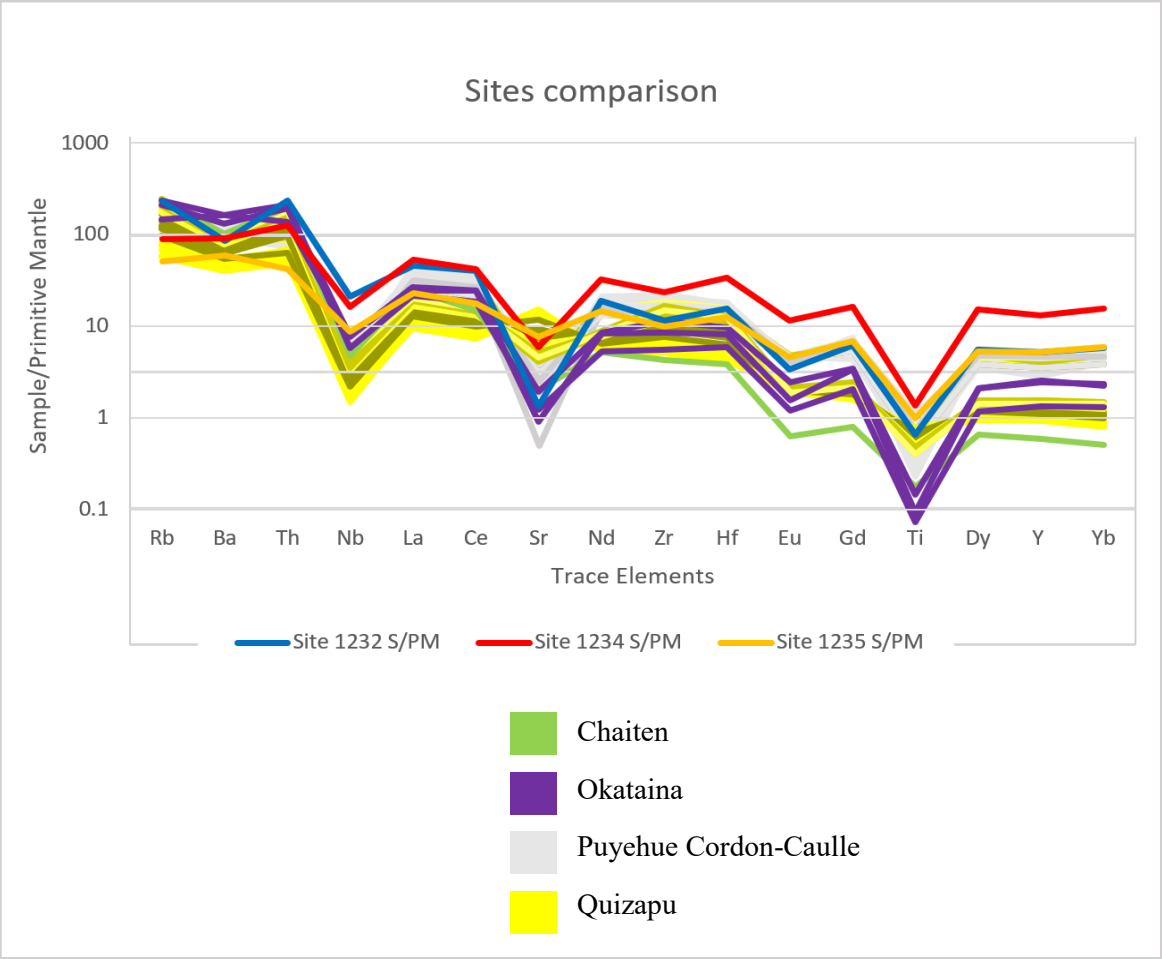

Figure 15. Spider diagram for sites 1232, 1234, and 1235 together with the plots of different volcanoes.

APPENDIX D

Volcano Name	Volcano Type	Year BP	Dating technique	Bulk deposit volume	Bulk DRE volume	Magma Type	Magnitude	VEI
Puyehue-Cordon Caulle	Stratovolcano(es)	1090	Radiocarbon (corrected)	3	1.28	Dacite	5	5
Puyehue-Cordon Caulle	Stratovolcano(es)	1090	Radiocarbon (corrected)	3	1.28	Dacite-Rhyolite	5	5
Maca	Stratovolcano(es)	1400	Radiocarbon (corrected)	1.7	0.68	Andesite	5.2	5
Antillanca Group	Stratovolcano(es)	2180	Radiocarbon (corrected)	3	1.2		5.5	5
Melimoyu	Stratovolcano(es)	2770	Radiocarbon (corrected)	0.6	0.24	Basalt-Dacite	4.8	5
Melimoyu	Stratovolcano(es)	2770	Radiocarbon (corrected)	0.6	0.24	Basalt-Dacite	4.8	5
Antillanca Group	Stratovolcano(es)	2910	Radiocarbon (corrected)	2	0.8	Andesite-Dacite	5	5
Antillanca Group	Stratovolcano(es)	2910	Radiocarbon (corrected)	2	0.8	Andesite-Dacite	5	5
Sollipulli	Caldera(s)	2927	Radiocarbon (corrected)	7.9	3.16	Not Available	5.9	5
Aguilera	Stratovolcano(es)	3200	Radiocarbon (corrected)	6	2.5	Dacite	5.8	5
Villarrica	Stratovolcano(es)	3800	Radiocarbon (corrected)	5	2	Andesite	5.7	5
Hudson, Cerro	Stratovolcano(es)	3840	Radiocarbon (corrected)	10	4	Trachyte	6	6
Hudson, Cerro	Stratovolcano(es)	3840	Radiocarbon (corrected)	10	4	Dacite	6	6
Burney, Monte	Stratovolcano(es)	4270	Radiocarbon (corrected)	2.8	1.16	Dacite	5.4	5
Chaiten	Caldera(s)	5050	Radiocarbon (corrected)	0.6	0.26	Rhyolite	4.8	5
Puyehue-Cordonn Caulle	Stratovolcano(es)	7030	Radiocarbon (corrected)	1	0.4		5	5
Minchinmavida	Stratovolcano(es)	7450	Radiocarbon (corrected)	0.6	0.24	Andesite	4.8	5
Mentolat	Stratovolcano(es)	7530	Radiocarbon (corrected)	1.4	0.56	Andesite	5.1	5
Corcovado	Stratovolcano(es)	7690	Radiocarbon (corrected)	1	0.4		5	5
Hudson, Cerro	Stratovolcano(es)	7710	Radiocarbon (corrected)	18	7.2	Trachyandesite	6.3	6
Hudson, Cerro	Stratovolcano(es)	7710	Radiocarbon (corrected)	18	7.2	Andesite	6.3	6
Burney, Monte	Stratovolcano(es)	9400	Radiocarbon (corrected)	3	1.25	Dacite	5.5	5
Chaiten	Caldera(s)	9700	Radiocarbon (corrected)	3.54	1.54	Rhyolite	5.5	5
Llaima	Stratovolcano(es)	9918	Radiocarbon (corrected)	4	1.54	Basalt-Andesite	4.7	5
Llaima	Stratovolcano(es)	9918	Radiocarbon (corrected)	4	1.54	Andesite-Dacite	4.7	5
Llaima	Stratovolcano(es)	9918	Radiocarbon (corrected)	4	1.54	Andesite-Dacite	4.7	5
Llaima	Stratovolcano(es)	9918	Radiocarbon (corrected)	4	1.54	Basalt-Andesite	4.7	5
Mocho-Choshuenco	Stratovolcano(es)	10300	Not Available	5.3	2.3	Rhyolite	5.7	5
Mocho-Choshuenco	Stratovolcano(es)	10300	Not Available	5.3	2.3	Dacite	5.7	5
Yanteles	Stratovolcano(es)	10364	Radiocarbon (corrected)	0.6	0.24	Andesite	4.8	5
Minchinmavida	Stratovolcano(es)	10380	Radiocarbon (corrected)	10	4	Andesite	6	6
Villarrica	Stratovolcano(es)	13800	Radiocarbon (corrected)	10	4	Basalt-Andesite	6	6
Villarrica	Stratovolcano(es)	13800	Radiocarbon (corrected)	10	4	Basalt-Andesite	6	6
Villarrica	Stratovolcano(es)	13800	Radiocarbon (corrected)	10	4	Andesite	6	6
Reclus	Cinder cone(s)	14600	Not Available	1	0.4		5	5
Reclus	Cinder cone(s)	14817	Radiocarbon (corrected)	10	4	Andesite	6	6
Llaima	Stratovolcano(es)	15991	Radiocarbon (corrected)	24	9.6	Basalt-Andesite	6.4	6
Llaima	Stratovolcano(es)	15991	Radiocarbon (corrected)	24	9.6	Andesite	6.4	6
Llaima	Stratovolcano(es)	15991	Radiocarbon (corrected)	24	9.6	Basalt-Andesite	6.4	6
Hudson, Cerro	Stratovolcano(es)	17370	Radiocarbon (corrected)	20	8.3	Trachyandesite-Trachyte	6.3	6
Hudson, Cerro	Stratovolcano(es)	17370	Radiocarbon (corrected)	20	8.3	Trachyandesite-Trachyte	6.3	6
Chillan, Nevados de	Stratovolcano(es)	42565	Radiocarbon (corrected)	10	4	Andesite	6	6
Villarrica	Stratovolcano(es)	95000	Not Available	10	4		6	6
Hudson, Cerro	Stratovolcano(es)	110000	K Ar	3	1.154	Basalt-Andesite	5.5	7
Hudson, Cerro	Stratovolcano(es)	110000	K Ar	3	1.154	Basalt-Andesite	5.5	7
Puyehue-Cordon Caulle	Stratovolcano(es)	121000	Stratigraphy	20	7.84	Basalt-Dacite	7.1	7
Puyehue-Cordon Caulle	Stratovolcano(es)	121000	Stratigraphy	20	7.84	Basalt-Dacite	7.1	7
Calabozos	Caldera(s)	150000	K Ar	225	93.75	Dacite	7.4	7
Calabozos	Caldera(s)	300000	Not Available	225	93.75	Dacite	7.4	7
Maipo	Caldera(s)	450000	Not Available	450	152.5	Rhyolite	7.7	7
Copahue	Stratovolcano(es)	500000	Not Available	100	40	Andesite	7	7
Calabozos	Caldera(s)	800000	Not Available	225	93.75	Dacite	7.4	7
Calabozos	Caldera(s)	810000	K Ar	1.5	0.63	Dacite	5.2	5

Table.1. Data of volcanic eruptions in Chile from the Pleistocene epoch to recent.

Volcano Name	Volcano Type	Year BP	Dating technique	Bulk deposit volume	Bulk DRE volume	Magma Type	Magnitude	VEI
Krakatau	Caldera(s)	1534	Historical records	0.1	0.04	Rhyolite	7.1	6
Merapi	Stratovolcano(es)	1930	Radiocarbon (corrected)	0.1	0.04	Not Available	4	4
Tengger Caldera	Stratovolcano(es)	2814	Radiocarbon (corrected)	0.1	0.04	Andesite	4	4
Merapi	Stratovolcano(es)	3274	Radiocarbon (corrected)	0.1	0.04	Not Available	4	4
Parker	Stratovolcano(es)	4323	Radiocarbon (corrected)	0.1	0.04	Not Available	4	4
Galunggung	Stratovolcano(es)	4645	Radiocarbon (corrected)	1	0.4	Not Available	5	5
Dieng Volcanic Complex	Complex volcano(es)	19233	Radiocarbon (corrected)	78	30	Andesite	6.9	6
Batur	Caldera(s)	24380	Radiocarbon (corrected)	10	5.5	Andesite-Dacite	6.1	6
Batur	Caldera(s)	24380	Radiocarbon (corrected)	10	5.5	Andesite-Dacite	6.1	6
Batur	Caldera(s)	34565	Radiocarbon (corrected)	27	18	Dacite	7.4	7
Tengger Caldera	Stratovolcano(es)	38249	Radiocarbon (corrected)	0.1	0.04	Not Available	4	4
Tambora	Stratovolcano(es)	43000	Other technique	0.1	0.04	Not Available	4	4
Maninjau	Caldera(s)	52000	Other technique	235	175	Andesite	7.2	7
Toba	Caldera(s)	74000	Other technique	2800	2750	Dacite-Rhyolite	8.8	8
Toba	Caldera(s)	74000	Other technique	2800	2750	Dacite-Rhyolite	8.8	8
Tangkubanparahu	Stratovolcano(es)	108358	Radiocarbon and stratigraphy	0.1	0.04	Not Available	4	4
Tengger Caldera	Stratovolcano(es)	152000	K Ar	3.79	1.52	Not Available	5.6	5
Tangkubanparahu	Stratovolcano(es)	190000	Not Available	10	4		6	6
Maninjau	Caldera(s)	280000	K Ar	175	70	Andesite-Rhyolite	7	7
Maninjau	Caldera(s)	280000	K Ar	175	70	Andesite-Rhyolite	7	7
Toba	Caldera(s)	501000	Ar-Ar	60	26.09	Rhyolite	7.1	7
Ranau	Caldera(s)	550000	K Ar	100	40	Rhyolite	7	7
Toba	Caldera(s)	840000	Not Available	820	800	Dacite-Rhyolite	8.4	8
Toba	Caldera(s)	840000	Not Available	820	800	Dacite-Rhyolite	8.4	8
Toba	Caldera(s)	1200000	ITPFT isothermal plateau fission track age	80.5	35	Dacite	8	6

Table 2. Data of volcanic eruptions in Indonesia from the Pleistocene epoch to recent.

Volcano Name	Volcano Type	Year BP	Dating technique	Bulk deposit volume	Bulk DRE volume	Magma Type	Magnitude	VEI
Healy	Submarine volcano(es)	590	Radiocarbon (corrected)	12.5	3	Dacite	5.9	5
Okataina	Lava dome(s)	640	Radiocarbon (corrected)	15.85	7.9	Rhyolite	6.3	5
Okataina	Lava dome(s)	640	Radiocarbon (corrected)	15.85	7.9	Rhyolite	6.3	5
Taupo	Caldera(s)	1720	Radiocarbon (corrected)	30	10	Rhyolite	6.9	6
Tongariro	Stratovolcano(es)	2500	Radiocarbon (corrected)	1	0.48	Not Available	5.1	5
Taupo	Caldera(s)	3410	Radiocarbon (corrected)	20	7.1	Rhyolite	6.2	6
Taranaki [Egmont]	Stratovolcano(es)	3904	Radiocarbon (corrected)	2	0.8		5	5
Okataina	Lava dome(s)	5530	Radiocarbon (corrected)	2.8	0.87	Rhyolite	6	5
Mayor Island	Shield volcano(es)	7010	Radiocarbon (corrected)	5.5	2.39	Rhyolite	5.7	5
Okataina	Lava dome(s)	8010	Radiocarbon (corrected)	6	2.609	Rhyolite	5.8	5
Okataina	Lava dome(s)	9510	Radiocarbon (corrected)	5.6	2.43	Rhyolite	5.7	5
Taupo	Caldera(s)	10080	Radiocarbon (corrected)	4.6	1.4		5.5	5
Taupo	Caldera(s)	11190	Radiocarbon (corrected)	3	0.23	Rhyolite	5.4	5
Tongariro	Stratovolcano(es)	11300	Tephrochronology	0.8	0.32		4	5
Tongariro	Stratovolcano(es)	11400	Radiocarbon (corrected)	0.4	0.16	Andesite-Dacite	4.9	5
Tongariro	Stratovolcano(es)	11400	Radiocarbon (corrected)	0.4	0.16	Andesite-Dacite	4.9	5
Taupo	Caldera(s)	11410	Radiocarbon (corrected)	1.3	0.42	Rhyolite	5	5
Tongariro	Stratovolcano(es)	11600	Radiocarbon (corrected)	0.2	0.07	Andesite-Rhyolite	4.6	5
Tongariro	Stratovolcano(es)	11600	Radiocarbon (corrected)	0.2	0.07	Andesite-Rhyolite	4.6	5
Okataina	Lava dome(s)	13598	Radiocarbon (corrected)	18	11	Rhyolite	6.4	6
Okataina	Lava dome(s)	15425	Radiocarbon (corrected)	7	1	Rhyolite	5.4	5
Okataina	Lava dome(s)	17625	Radiocarbon (corrected)	7	5	Rhyolite	6.1	6
Yasur	Stratovolcano(es)	20000	Not Available	1	0.4	Not Available	5	5
Okataina	Lava dome(s)	21800	Radiocarbon (corrected)	6	3.6	Rhyolite	5.9	6
Taranaki [Egmont]	Stratovolcano(es)	23649	Radiocarbon (corrected)	1.88	0.75	Andesite	5.3	5
Okataina	Lava dome(s)	25271	Radiocarbon (corrected)	5	13	Rhyolite	6.5	6
Taupo	Caldera(s)	27100	Radiocarbon (corrected)	1170	530	Rhyolite	8.1	8
Taupo	Caldera(s)	28181	Radiocarbon (corrected)	1	0.5	Rhyolite	5	5
Taupo	Caldera(s)	30092	Radiocarbon (corrected)	6	3	Rhyolite	5.8	5
Okataina	Lava dome(s)	31400	Radiocarbon (corrected)	4.3	1.3		5.5	5
Okataina	Lava dome(s)	32301	Radiocarbon (corrected)	16.2	4.1		6	6
Okataina	Lava dome(s)	32800	Radiocarbon (corrected)	0.77	0.23		4.7	5
Okataina	Lava dome(s)	33000	Radiocarbon (corrected)	19.9	6		6.2	6
Okataina	Lava dome(s)	35000	Radiocarbon (corrected)	2.5	0.63		5.2	5
Okataina	Lava dome(s)	36100	Radiocarbon (corrected)	15.2	3.9		6	6
Okataina	Lava dome(s)	36700	Radiocarbon (corrected)	0.9	0.34		4.9	5
Okataina	Lava dome(s)	36800	Radiocarbon (corrected)	11	2.8		5.8	6
Okataina	Lava dome(s)	39000	Radiocarbon (corrected)	4.6	1.2		5.4	5
Taupo	Caldera(s)	41000	Radiocarbon (corrected)	1	0.5	Rhyolite	5.1	5
Taupo	Caldera(s)	42000	Stratigraphy, sediment accumulation	4	2.2	Rhyolite	5.7	5
Taupo	Caldera(s)	42000	Radiocarbon (corrected)	2	1	Rhyolite	5.4	5
Taupo	Caldera(s)	46000	Stratigraphy	5	3		5.8	5
Taupo	Caldera(s)	55000	Stratigraphy	3.5	1.4		5	5
Kapenga	Caldera(s)	61000	Ar-Ar	15.5	7		6.4	6
Okataina	Lava dome(s)	61000	Ar-Ar	350	100	Rhyolite	7.4	7
Maroa	Caldera(s)	212500	Not Available	1	0.434	Rhyolite	5	5
Okataina	Lava dome(s)	225000	Not Available	100	40		7.5	7
Maroa	Caldera(s)	229000	Not Available	1	0.434	Rhyolite	5	5
Reporoa	Caldera(s)	230000	Ar-Ar	230	200	Rhyolite	7.4	7
Rotorua	Caldera(s)	230000	ITPFT isothermal plateau fission track age	339	145	Rhyolite	7.7	7
Maroa	Caldera(s)	256000	Not Available	2	0.868	Rhyolite	5.3	5
Kapenga	Caldera(s)	270000	ITPFT isothermal plateau fission track age	43.5	100		7.4	7
Maroa	Caldera(s)	272000	Not Available	2	0.868	Rhyolite	5.3	5
Kapenga	Caldera(s)	275000	Ar-Ar	230	100	Rhyolite	7.4	7
Okataina	Lava dome(s)	280000	Ar-Ar	345	150	Rhyolite	7.5	7
Maroa	Caldera(s)	283000	Not Available	1	0.434	Rhyolite	5	5
Maroa	Caldera(s)	325000	Ar-Ar	1150	500	Rhyolite	8	8
Kapenga	Caldera(s)	330000	ITPFT isothermal plateau fission track age	115	50	Rhyolite	7	7
Maroa	Caldera(s)	335000	Ar-Ar	1000	650	Rhyolite	8.2	8
Okataina	Lava dome(s)	340000	ITPFT isothermal plateau fission track age	25	10.9	Rhyolite	6.4	6
Okataina	Lava dome(s)	550000	Not Available	225	90		7	7
Kapenga	Caldera(s)	680000	Ar-Ar	150	65	Rhyolite	7.2	7
Kapenga	Caldera(s)	710000	Ar-Ar	460	200	Rhyolite	7.7	7
Kapenga	Caldera(s)	720000	Ar-Ar	69	30	Rhyolite	6.8	6
Kapenga	Caldera(s)	805000	Stratigraphy	149.5	65	Rhyolite	7.1	7
Kapenga	Caldera(s)	890000	Ar-Ar	69	30	Rhyolite	6.8	6
Mangakino	Caldera(s)	950000	Ar-Ar	115	50	Rhyolite	6.7	7
Mangakino	Caldera(s)	970000	Ar-Ar	300	200	Rhyolite	7.5	7
Mangakino	Caldera(s)	1000000	Ar-Ar	1495	650	Rhyolite	7.5	7
Mangakino	Caldera(s)	1000000	Not Available	1000	400		8	8
Mangakino	Caldera(s)	1010000	Ar-Ar	2760	1200	Rhyolite	8	8
Mangakino	Caldera(s)	1180000	Ar-Ar	230	100	Rhyolite	6.7	7
Mangakino	Caldera(s)	1200000	Ar-Ar	230	100	Rhyolite	6	7
Mangakino	Caldera(s)	1210000	Ar-Ar	920	400	Rhyolite	7.5	8
Mangakino	Caldera(s)	1240000	Ar-Ar	1000	400		8	8
Mangakino	Caldera(s)	1400000	Ar-Ar	115	50	Rhyolite	6	7
Mangakino	Caldera(s)	1530000	Ar-Ar	230	100	Rhyolite	7.4	7
Mangakino	Caldera(s)	1550000	Ar-Ar	460	200	Rhyolite	6.7	7
Taupo	Caldera(s)	1600000	K Ar	69	30	Rhyolite	6.8	6
Mangakino	Caldera(s)	1630000	Not Available	1000	400		8	8

Table 3. Data of volcanic eruptions in New Zealand from the Pleistocene epoch to recent.

APPENDIX E

A

Site 1232 ash layer in core 034X, section 03W, 116-117 cm

Element	ES4_1232_1 Average	ES4_1232_2 Average	ES4_1232_3	ES4_1232_4 Average	ES4_1232_5 Average	ES4_1232_6 Average	ES4_1232_7 Average	ES4_1232_8	ES4_1232_9 Average	ES4_1232_10
Ca42	3575.2	6443.72	2955.45	4706.19	2485.505	4939.52	3196.72	3590.93	3694.025	4072.66
Ca43	4288.21	7432.89	3759.33	4295.35	3173.27	4967.17	3416.27	4431.15	4038.06	3687.86
Ti49	114.235	270.265	108.43	150.37	79.055	141.225	87.32	106.52	95.955	109.83
Fe57	4893.085	10842.175	4587.68	6262.18	3334.755	6405.78	4152.92	5142.26	5162.365	6128.3
Rb85	145.38	325.54	139.77	194.045	101.805	189.88	126.66	160.13	148.455	175.63
Sr88	26.755	49.935	22.08	34.995	17.985	38.29	21.41	30.65	28.27	28.33
Y89	22.35	44.525	23.51	38.845	20.765	40.77	23.90	32.55	26.34	30.24
Zr90	120.535	257.66	123.11	198.165	108.1	210.05	123.14	169.08	139.005	168.06
Nb93	13.73	28.22	12.85	18.005	9.94	18.815	12.08	15.88	14.025	16.76
Ba137	563.045	1210.49	535.79	817.33	425.71	836.94	514.94	682.61	623.115	734.17
La139	29.45	64.345	30.03	48.59	24.955	50.065	30.13	42.62	35.37	40.19
Ce140	66.64	138.555	63.96	90.7	49.065	91.225	57.15	76.09	70.765	83
Nd146	23.69	50.55	24.84	39.315	20.58	40.255	23.93	33.41	28.97	31.36
Eu153	0.522	1.185	0.49	0.765	0.375	0.835	0.50	0.75	0.54	0.69
Gd157	3.35	8.26	3.67	5.625	3.565	6.74	3.98	5.15	4.45	5.12
Dy163	3.72	8.56	3.71	5.39	3.31	6.64	3.97	5.37	4.28	4.47
Yb174	2.55	5.775	2.55	4.365	2.305	4.805	2.94	3.70	3.195	3.59
Hf178	4.385	9.52	4.73	7.31	3.63	7.735	4.77	5.91	4.635	5.66
Th232	18.585	39.555	19.09	30.535	16.73	32.715	19.84	27.29	22.9	26.16

B

Site 1234 ash layer Core 003H, Section 03W, 49-50 cm

Element	ES1_1234_1 Average	ES1_1234_2	ES1_1234_3 Average	ES1_1234_4	ES1_1234_5	ES1_1234_6 Average	ES1_1234_7	ES1_1234_8	ES1_1234_9	ES1_1234_10 Average
Ca42	11589.205	9653.43	8862.39	11312.22	11524.25	10420.82	8847.61	8025.66	10400.46	12141.12
Ca43	12643.06	10277.4	9705.64	11906.92	11263.69	11871.18	10577.58	8454.91	12771.71	12485.83
Ti49	349.035	292.14	274.07	340.62	320.92	348.585	294.12	250.76	360.5	400.155
Fe57	8741.13	7167.67	6732.41	24148.92	8029.05	8358.88	7036.77	6124.25	8706.66	9566.01
Rb85	56.395	45.21	43.87	53.17	55.37	57.54	44.79	37.68	58.83	60.165
Sr88	118.34	95.96	90.035	115.68	109.41	108.75	92.79	83.42	114.73	122.875
Y89	56.235	47.75	42.595	57.84	59.79	56.77	47.02	45.98	62.67	57.41
Zr90	244.055	207.76	188.99	253.71	263.69	256.81	208.93	201.27	287.35	262.975
Nb93	10.615	8.4	8.25	10.86	10.32	11.225	8.35	6.99	10.79	12.425
Ba137	595.415	513.38	467.355	607.95	592.14	603.08	488.73	433.17	634.84	629.39
La139	34.525	28.75	26.41	33.98	34.8	34.34	28.13	27.04	37.46	36.04
Ce140	69.97	60.44	54.91	70.5	69.24	73.905	58.05	51.8	72.93	75.7
Nd146	40.14	34.59	31.16	40.83	39.21	40.84	33.99	32.72	41.59	42.18
Eu153	1.775	1.35	1.245	1.81	1.7	1.665	1.16	1.32	1.6	1.63
Gd157	8.86	7.68	7.125	9.26	9.37	9.14	7.05	6.41	9.99	8.985
Dy163	10.27	8.94	7.8	10.71	9.88	10.28	8.05	7.38	12	10.33
Yb174	6.92	6.03	5.25	6.86	7.17	6.97	5.73	5.25	7.67	7.515
Hf178	9.56	8.06	7.065	10.78	10.28	9.74	7.47	8.1	10.84	9.62
Th232	9.88	8.76	7.63	10.48	10.45	10.04	7.91	7.57	10.79	10.31

C

Site 1235 ash layer Core 04H, Section 05W, 120-121.5 cm

----------	ES3_1235_1 Average	ES3_1235_2 Average	ES3_1235_3 Average	ES3_1235_4	ES3_1235_5	ES3_1235_6	ES3_1235_7	ES3_1235_8 Average	ES3_1235_9	ES3_1235_10
Ca42	10402.725	9301.91	10254.935	9259.72	12238.04	12699.68	7998.18	9641.075	11738.22	9349.3
Ca43	11785.42	10091.58	9877.17	9276.82	11778.27	12550.15	8176.18	12085.59	12928.94	11070.72
Ti49	174.53	138.265	140.3	141.99	170.35	142.25	95.01	113.045	138.83	120.16
Fe57	6986.005	5762.035	6285.2	5906.3	8398.99	7910.4	5202.43	6443.815	7561.62	6739.44
Rb85	32.07	28.48	31.49	28.25	38.06	38.09	25.27	33.565	37.67	33.76
Sr88	152.365	135.12	139.055	133.28	173.18	175.24	106.51	142.765	171.25	138.75
Y89	22.325	19.395	21.53	17.78	23.34	24	13.53	20.01	23.73	18.97
Zr90	104.1	89.525	95.2	88.24	110.55	116.74	69.98	99.94	110.13	89.17
Nb93	5.735	4.65	5.05	4.78	6.1	6.45	3.6	5.515	6.57	5.03
Ba137	392.21	356.5	376.715	353.55	482.72	479.69	296.84	398.375	483.02	409.19
La139	14.98	13.335	13.565	12.94	16.55	17.62	10.74	14.045	17.76	13.6
Ce140	29.79	26.67	27.48	24.75	34.94	34.83	23.64	30.095	36.55	29.57
Nd146	18.275	16.675	15.71	16.9	20.69	20.26	12.47	16.785	20.44	16.84
Eu153	0.705	0.589	0.635	0.65	0.81	0.74	0.532	0.655	0.78	0.72
Gd157	3.73	3.84	3.125	3.47	3.57	4.61	2.28	3.125	3.93	4.1
Dy163	3.585	3.415	3.26	3.34	4.1	4.18	2.75	3.52	4.2	3.58
Yb174	2.575	1.95	2.075	2.03	2.2	2.99	1.68	2.065	2.19	2.01
Hf178	3.535	3.18	2.85	3.06	3.47	4.03	2.4	3.28	4.01	3.47
Th232	3.36	2.9	3.15	2.99	4.05	3.93	2.3	3.235	3.66	2.86

Table 4. Concentrations in Parts Per Million (PPM) of trace elements. Raw values collected from the LA ICP-MS. A. Site 1232 B. Site 1234 C. Site 1235.

APPENDIX F

Tables of the concentrations (in parts per million) of trace elements plotted in x-y graphs.

1232		1234		1235	
Ti49	Y89	Ti49	Y89	Ti49	Y89
114.235	22.35	349.035	56.235	174.53	22.325
270.265	44.525	292.14	47.75	138.265	19.395
108.43	23.51	274.07	42.595	140.3	21.53
150.37	38.845	340.62	57.84	141.99	17.78
79.055	20.765	320.92	59.79	170.35	23.34
141.225	40.77	348.585	56.77	142.25	24
87.32	23.90	294.12	47.02	95.01	13.53
106.52	32.55	250.76	45.98	113.045	20.01
95.955	26.34	360.5	62.67	138.83	23.73
109.83	30.24	400.155	57.41	120.16	18.97

Table 5a. Concentrations of Ti and Y for sites 1232, 1234, and 1235.

1232		1234		1235	
Ti49	Zr90	Ti49	Zr90	Ti49	Zr90
114.235	120.535	349.035	244.055	174.53	104.1
270.265	257.66	292.14	207.76	138.265	89.525
108.43	123.11	274.07	188.99	140.3	95.2
150.37	198.165	340.62	253.71	141.99	88.24
79.055	108.1	320.92	263.69	170.35	110.55
141.225	210.05	348.585	256.81	142.25	116.74
87.32	123.14	294.12	208.93	95.01	69.98
106.52	169.08	250.76	201.27	113.045	99.94
95.955	139.005	360.5	287.35	138.83	110.13
109.83	168.06	400.155	262.975	120.16	89.17

Table 5b. Concentrations of Ti and Zr for sites 1232, 1234, and 1235.

1232		1234		1235	
Sr88	Y89	Sr88	Y89	Sr88	Y89
26.755	22.35	118.34	56.235	152.365	22.325
49.935	44.525	95.96	47.75	135.12	19.395
22.08	23.51	90.035	42.595	139.055	21.53
34.995	38.845	115.68	57.84	133.28	17.78
17.985	20.765	109.41	59.79	173.18	23.34
38.29	40.77	108.75	56.77	175.24	24
21.41	23.90	92.79	47.02	106.51	13.53
30.65	32.55	83.42	45.98	142.765	20.01
28.27	26.34	114.73	62.67	171.25	23.73
28.33	30.24	122.875	57.41	138.75	18.97

Table 5c. Concentrations of Sr and Y for sites 1232, 1234, and 1235.

1232		1234		1235	
La139	Y89	La139	Y89	La139	Y89
29.45	22.35	34.525	56.235	14.98	22.325
64.345	44.525	28.75	47.75	13.335	19.395
30.03	23.51	26.41	42.595	13.565	21.53
48.59	38.845	33.98	57.84	12.94	17.78
24.955	20.765	34.8	59.79	16.55	23.34
50.065	40.77	34.34	56.77	17.62	24
30.13	23.90	28.13	47.02	10.74	13.53
42.62	32.55	27.04	45.98	14.045	20.01
35.37	26.34	37.46	62.67	17.76	23.73
40.19	30.24	36.04	57.41	13.6	18.97

Table 5d. Cocentrations of La and Y for sites 1232, 1234, and 1235.

1232		1234		1235	
La139	Yb174	La139	Yb174	La139	Yb174
29.45	2.55	34.525	6.92	14.98	2.575
64.345	5.775	28.75	6.03	13.335	1.95
30.03	2.55	26.41	5.25	13.565	2.075
48.59	4.365	33.98	6.86	12.94	2.03
24.955	2.305	34.8	7.17	16.55	2.2
50.065	4.805	34.34	6.97	17.62	2.99
30.13	2.94	28.13	5.73	10.74	1.68
42.62	3.70	27.04	5.25	14.045	2.065
35.37	3.195	37.46	7.67	17.76	2.19
40.19	3.59	36.04	7.515	13.6	2.01

Table 5e. Concentrations of La and Yb for sites 1232, 1234, and 1235.

1232		1234		1235	
La139	Nb93	La139	Nb93	La139	Nb93
29.45	13.73	34.525	10.615	14.98	5.735
64.345	28.22	28.75	8.4	13.335	4.65
30.03	12.85	26.41	8.25	13.565	5.05
48.59	18.005	33.98	10.86	12.94	4.78
24.955	9.94	34.8	10.32	16.55	6.1
50.065	18.815	34.34	11.225	17.62	6.45
30.13	12.08	28.13	8.35	10.74	3.6
42.62	15.88	27.04	6.99	14.045	5.515
35.37	14.025	37.46	10.79	17.76	6.57
40.19	16.76	36.04	12.425	13.6	5.03

Table 5f. Concentrations of La and Nb for sites 1232, 1234, and 1235.

1232		1234		1235	
Zr90	Nb93	Zr90	Nb93	Zr90	Nb93
120.535	13.73	244.055	10.615	104.1	5.735
257.66	28.22	207.76	8.4	89.525	4.65
123.11	12.85	188.99	8.25	95.2	5.05
198.165	18.005	253.71	10.86	88.24	4.78
108.1	9.94	263.69	10.32	110.55	6.1
210.05	18.815	256.81	11.225	116.74	6.45
123.14	12.08	208.93	8.35	69.98	3.6
169.08	15.88	201.27	6.99	99.94	5.515
139.005	14.025	287.35	10.79	110.13	6.57
168.06	16.76	262.975	12.425	89.17	5.03

Table 5g. Concentrations of Zr and Nb for sites 1232, 1234, and 1235.

1232		1234		1235	
Zr90	Y89	Zr90	Y89	Zr90	Y89
120.535	22.35	244.055	56.235	104.1	22.325
257.66	44.525	207.76	47.75	89.525	19.395
123.11	23.51	188.99	42.595	95.2	21.53
198.165	38.845	253.71	57.84	88.24	17.78
108.1	20.765	263.69	59.79	110.55	23.34
210.05	40.77	256.81	56.77	116.74	24
123.14	23.90	208.93	47.02	69.98	13.53
169.08	32.55	201.27	45.98	99.94	20.01
139.005	26.34	287.35	62.67	110.13	23.73
168.06	30.24	262.975	57.41	89.17	18.97

Table 5h. Concentrations of Zr and Y for sites 1232, 1234, and 1235.

1232		1234		1235	
Ba137	La139	Ba137	La139	Ba137	La139
563.045	29.45	595.415	34.525	392.21	14.98
1210.49	64.345	513.38	28.75	356.5	13.335
535.79	30.03	467.355	26.41	376.715	13.565
817.33	48.59	607.95	33.98	353.55	12.94
425.71	24.955	592.14	34.8	482.72	16.55
836.94	50.065	603.08	34.34	479.69	17.62
514.94	30.13	488.73	28.13	296.84	10.74
682.61	42.62	433.17	27.04	398.375	14.045
623.115	35.37	634.84	37.46	483.02	17.76
734.17	40.19	629.39	36.04	409.19	13.6

Table 5i. Concentrations of Ba and La for sites 1232, 1234, and 1235.

1232		1234		1235	
Ba137	Th232	Ba137	Th232	Ba137	Th232
563.045	18.585	595.415	9.88	392.21	3.36
1210.49	39.555	513.38	8.76	356.5	2.9
535.79	19.09	467.355	7.63	376.715	3.15
817.33	30.535	607.95	10.48	353.55	2.99
425.71	16.73	592.14	10.45	482.72	4.05
836.94	32.715	603.08	10.04	479.69	3.93
514.94	19.84	488.73	7.91	296.84	2.3
682.61	27.29	433.17	7.57	398.375	3.235
623.115	22.9	634.84	10.79	483.02	3.66
734.17	26.16	629.39	10.31	409.19	2.86

Table 5j. Concentrations of Ba and Th for sites 1232, 1234, and 1235.

1232		1234		1235	
Th232	La139	Th232	La139	Th232	La139
18.585	29.45	9.88	34.525	3.36	14.98
39.555	64.345	8.76	28.75	2.9	13.335
19.09	30.03	7.63	26.41	3.15	13.565
30.535	48.59	10.48	33.98	2.99	12.94
16.73	24.955	10.45	34.8	4.05	16.55
32.715	50.065	10.04	34.34	3.93	17.62
19.84	30.13	7.91	28.13	2.3	10.74
27.29	42.62	7.57	27.04	3.235	14.045
22.9	35.37	10.79	37.46	3.66	17.76
26.16	40.19	10.31	36.04	2.86	13.6

Table 5k. Concentrations of Th and La for sites 1232, 1234, and 1235.

1232		1234		1235	
Zr90	Hf178	Zr90	Hf178	Zr90	Hf178
120.535	4.385	244.055	9.56	104.1	3.535
257.66	9.52	207.76	8.06	89.525	3.18
123.11	4.73	188.99	7.065	95.2	2.85
198.165	7.31	253.71	10.78	88.24	3.06
108.1	3.63	263.69	10.28	110.55	3.47
210.05	7.735	256.81	9.74	116.74	4.03
123.14	4.77	208.93	7.47	69.98	2.4
169.08	5.91	201.27	8.1	99.94	3.28
139.005	4.635	287.35	10.84	110.13	4.01
168.06	5.66	262.975	9.62	89.17	3.47

Table 5l. Concentrations of Zr and Hf for sites 1232, 1234, and 1235.

1232		1234		1235	
Zr90	La139	Zr90	La139	Zr90	La139
120.535	29.45	244.055	34.525	104.1	14.98
257.66	64.345	207.76	28.75	89.525	13.335
123.11	30.03	188.99	26.41	95.2	13.565
198.165	48.59	253.71	33.98	88.24	12.94
108.1	24.955	263.69	34.8	110.55	16.55
210.05	50.065	256.81	34.34	116.74	17.62
123.14	30.13	208.93	28.13	69.98	10.74
169.08	42.62	201.27	27.04	99.94	14.045
139.005	35.37	287.35	37.46	110.13	17.76
168.06	40.19	262.975	36.04	89.17	13.6

Table 5m. Concentrations of Zr and La for sites 1232, 1234, and 1235.

1232		1234		1235	
Zr90	Nd146	Zr90	Nd146	Zr90	Nd146
120.535	23.69	244.055	40.14	104.1	18.275
257.66	50.55	207.76	34.59	89.525	16.675
123.11	24.84	188.99	31.16	95.2	15.71
198.165	39.315	253.71	40.83	88.24	16.9
108.1	20.58	263.69	39.21	110.55	20.69
210.05	40.255	256.81	40.84	116.74	20.26
123.14	23.93	208.93	33.99	69.98	12.47
169.08	33.41	201.27	32.72	99.94	16.785
139.005	28.97	287.35	41.59	110.13	20.44
168.06	31.36	262.975	42.18	89.17	16.84

Table 5n. Concentrations of Zr and Nd for sites 1232, 1234, and 1235.

1232		1234		1235	
La139	Gd157	La139	Gd157	La139	Gd157
29.45	3.35	34.525	8.86	14.98	3.73
64.345	8.26	28.75	7.68	13.335	3.84
30.03	3.67	26.41	7.125	13.565	3.125
48.59	5.625	33.98	9.26	12.94	3.47
24.955	3.565	34.8	9.37	16.55	3.57
50.065	6.74	34.34	9.14	17.62	4.61
30.13	3.98	28.13	7.05	10.74	2.28
42.62	5.15	27.04	6.41	14.045	3.125
35.37	4.45	37.46	9.99	17.76	3.93
40.19	5.12	36.04	8.985	13.6	4.1

Table 5o. Concentrations of La and Gd for sites 1232, 1234, and 1235.

1232		1234		1235	
Gd157	Yb174	Gd157	Yb174	Gd157	Yb174
3.35	2.55	8.86	6.92	3.73	2.575
8.26	5.775	7.68	6.03	3.84	1.95
3.67	2.55	7.125	5.25	3.125	2.075
5.625	4.365	9.26	6.86	3.47	2.03
3.565	2.305	9.37	7.17	3.57	2.2
6.74	4.805	9.14	6.97	4.61	2.99
3.98	2.94	7.05	5.73	2.28	1.68
5.15	3.70	6.41	5.25	3.125	2.065
4.45	3.195	9.99	7.67	3.93	2.19
5.12	3.59	8.985	7.515	4.1	2.01

Table 5p. Concentrations of Gd and Yb for sites 1232, 1234, and 1235.

1232		1234		1235	
Dy163	Yb174	Dy163	Yb174	Dy163	Yb174
3.72	2.55	10.27	6.92	3.585	2.575
8.56	5.775	8.94	6.03	3.415	1.95
3.71	2.55	7.8	5.25	3.26	2.075
5.39	4.365	10.71	6.86	3.34	2.03
3.31	2.305	9.88	7.17	4.1	2.2
6.64	4.805	10.28	6.97	4.18	2.99
3.97	2.94	8.05	5.73	2.75	1.68
5.37	3.70	7.38	5.25	3.52	2.065
4.28	3.195	12	7.67	4.2	2.19
4.47	3.59	10.33	7.515	3.58	2.01

Table 5q. Concentrations of Dy and Yb for sites 1232, 1234, and 1235.

APPENDIX G

Data utilized to create the oxide vs trace elements plots.

1232					
SiO2	Zr90	La139	Nb93	Ba137	Nd146
75.6074	120.535	29.45	13.73	563.045	23.69
76.3202	257.66	64.345	28.22	1210.49	50.55
75.6596	123.11	30.03	12.85	535.79	24.84
76.1133	198.165	48.59	18.005	817.33	39.315
76.092	108.1	24.955	9.94	425.71	20.58
75.9181	210.05	50.065	18.815	836.94	40.255
76.1915	123.14	30.13	12.08	514.94	23.93
75.692	169.08	42.62	15.88	682.61	33.41
75.447	139.005	35.37	14.025	623.115	28.97
76.094	168.06	40.19	16.76	734.17	31.36

Table 6a. Concentrations of SiO2 and Zr, La, Nb, Ba, and Nd for site 1232.

1234					
SiO2	Zr90	La139	Nb93	Ba137	Nd146
71.5878	244.055	34.525	10.615	595.415	40.14
71.0745	207.76	28.75	8.4	513.38	34.59
71.6362	188.99	26.41	8.25	467.355	31.16
70.8048	253.71	33.98	10.86	607.95	40.83
71.2851	263.69	34.8	10.32	592.14	39.21
71.7489	256.81	34.34	11.225	603.08	40.84
71.2101	208.93	28.13	8.35	488.73	33.99
72.0447	201.27	27.04	6.99	433.17	32.72
71.7904	287.35	37.46	10.79	634.84	41.59
71.7516	262.975	36.04	12.425	629.39	42.18

Table 6b. Concentrations of SiO2 and Zr, La, Nb, Ba, and Nd for site 1234.

1235					
SiO2	Zr90	La139	Nb93	Ba137	Nd146
77.5356	104.1	14.98	5.735	392.21	18.275
79.6245	89.525	13.335	4.65	356.5	16.675
78.9617	95.2	13.565	5.05	376.715	15.71
78.3729	88.24	12.94	4.78	353.55	16.9

Table 6c. Concentrations of SIO2 and Zr, La, Nb, Ba, and Nd for site 1235.

APPENDIX H

Concentrations of trace elements from samples along with the recommended values as established by McDonough and Sun (1995). The Multi-element plots are created by dividing the sample concentrations by the recommended values.

1				2				3				4				5			
Site 1232				Site 1232				Site 1232				Site 1232				Site 1232			
Elements	S/PM	Primitive Mantle	Samples	Elements	S/PM	Primitive Mantle	Samples	Elements	S/PM	Primitive Mantle	Samples	Elements	S/PM	Primitive Mantle	Samples	Elements	S/PM	Primitive Mantle	Samples
Rb	228.9449	0.635	145.38	Rb	512.6614	0.635	325.54	Rb	512.6614	0.635	325.54	Rb	305.5827	0.635	194.045	Rb	160.3228	0.635	101.805
Ba	85.30985	6.6	563.045	Ba	183.4076	6.6	1210.49	Ba	183.4076	6.6	1210.49	Ba	123.8379	6.6	817.33	Ba	64.50152	6.6	425.71
Th	233.7736	0.0795	18.585	Th	497.5472	0.0795	39.555	Th	497.5472	0.0795	39.555	Th	384.0881	0.0795	30.535	Th	210.4403	0.0795	16.73
Nb	20.86626	0.658	13.73	Nb	42.88754	0.658	28.22	Nb	42.88754	0.658	28.22	Nb	27.36322	0.658	18.005	Nb	15.10638	0.658	9.94
La	45.44753	0.648	29.45	La	99.29784	0.648	64.345	La	99.29784	0.648	64.345	La	74.98457	0.648	48.59	La	38.5108	0.648	24.955
Ce	39.78507	1.675	66.64	Ce	82.7194	1.675	138.555	Ce	82.7194	1.675	138.555	Ce	54.14925	1.675	90.7	Ce	29.29254	1.675	49.065
Sr	1.344472	19.9	26.755	Sr	2.509296	19.9	49.935	Sr	2.509296	19.9	49.935	Sr	1.758543	19.9	34.995	Sr	0.903769	19.9	17.985
Nd	18.952	1.25	23.69	Nd	40.44	1.25	50.55	Nd	40.44	1.25	50.55	Nd	31.452	1.25	39.315	Nd	16.464	1.25	20.58
Zr	11.47952	10.5	120.535	Zr	24.53905	10.5	257.66	Zr	24.53905	10.5	257.66	Zr	18.87286	10.5	198.165	Zr	10.29524	10.5	108.1
Hf	15.4947	0.283	4.385	Hf	33.63958	0.283	9.52	Hf	33.63958	0.283	9.52	Hf	25.83039	0.283	7.31	Hf	12.82686	0.283	3.63
Eu	3.38961	0.154	0.522	Eu	7.694805	0.154	1.185	Eu	7.694805	0.154	1.185	Eu	4.967532	0.154	0.765	Eu	2.435065	0.154	0.375
Gd	6.158088	0.544	3.35	Gd	15.18382	0.544	8.26	Gd	15.18382	0.544	8.26	Gd	10.34007	0.544	5.625	Gd	6.553309	0.544	3.565
Ti	0.094801	1205	114.235	Ti	0.224286	1205	270.265	Ti	0.224286	1205	270.265	Ti	0.124788	1205	150.37	Ti	0.065606	1205	79.055
Dy	5.519288	0.674	3.72	Dy	12.7003	0.674	8.56	Dy	12.7003	0.674	8.56	Dy	7.997033	0.674	5.39	Dy	4.910979	0.674	3.31
Y	5.197674	4.3	22.35	Y	10.35465	4.3	44.525	Y	10.35465	4.3	44.525	Y	9.033721	4.3	38.845	Y	4.82907	4.3	20.765
Yb	5.782313	0.441	2.55	Yb	13.09524	0.441	5.775	Yb	13.09524	0.441	5.775	Yb	9.897959	0.441	4.365	Yb	5.226757	0.441	2.305
6				7				8				9				10			
Site 1232				Site 1232				Site 1232				Site 1232				Site 1232			
Elements	S/PM	Primitive Mantle	Samples	Elements	S/PM	Primitive Mantle	Samples	Elements	S/PM	Primitive Mantle	Samples	Elements	S/PM	Primitive Mantle	Samples	Elements	S/PM	Primitive Mantle	Samples
Rb	299.0236	0.635	189.88	Rb	199.4646	0.635	126.66	Rb	252.1732	0.635	160.13	Rb	233.7874	0.635	148.455	Rb	276.5827	0.635	175.63
Ba	126.8091	6.6	836.94	Ba	78.02121	6.6	514.94	Ba	103.4258	6.6	682.61	Ba	94.41136	6.6	623.115	Ba	111.2379	6.6	734.17
Th	411.5094	0.0795	32.715	Th	249.5178	0.0795	19.83667	Th	343.2704	0.0795	27.29	Th	288.0503	0.0795	22.9	Th	329.0566	0.0795	26.16
Nb	28.59422	0.658	18.815	Nb	18.36373	0.658	12.08333	Nb	24.13374	0.658	15.88	Nb	21.31459	0.658	14.025	Nb	25.47112	0.658	16.76
La	77.2608	0.648	50.065	La	46.49177	0.648	30.12667	La	65.7716	0.648	42.62	La	54.58333	0.648	35.37	La	62.0216	0.648	40.19
Ce	54.46269	1.675	91.225	Ce	34.11741	1.675	57.14667	Ce	45.42687	1.675	76.09	Ce	42.24776	1.675	70.765	Ce	49.55224	1.675	83
Sr	1.924121	19.9	38.29	Sr	1.076047	19.9	21.41333	Sr	1.540201	19.9	30.65	Sr	1.420603	19.9	28.27	Sr	1.423618	19.9	28.33
Nd	32.204	1.25	40.255	Nd	19.144	1.25	23.93	Nd	26.728	1.25	33.41	Nd	23.176	1.25	28.97	Nd	25.088	1.25	31.36
Zr	20.00476	10.5	210.05	Zr	11.72762	10.5	123.14	Zr	16.10286	10.5	169.08	Zr	13.23857	10.5	139.005	Zr	16.00571	10.5	168.06
Hf	27.33216	0.283	7.735	Hf	16.85512	0.283	4.77	Hf	20.88339	0.283	5.91	Hf	16.37809	0.283	4.635	Hf	20	0.283	5.66
Eu	5.422078	0.154	0.835	Eu	3.264069	0.154	0.502667	Eu	4.87013	0.154	0.75	Eu	3.506494	0.154	0.54	Eu	4.480519	0.154	0.69
Gd	12.38971	0.544	6.74	Gd	7.310049	0.544	3.976667	Gd	9.466912	0.544	5.15	Gd	8.180147	0.544	4.45	Gd	9.411765	0.544	5.12
Ti	0.117199	1205	141.225	Ti	0.072465	1205	87.32	Ti	0.088398	1205	106.52	Ti	0.079631	1205	95.955	Ti	0.091145	1205	109.83
Dy	9.851632	0.674	6.64	Dy	5.895153	0.674	3.973333	Dy	7.967359	0.674	5.37	Dy	6.350148	0.674	4.28	Dy	6.632047	0.674	4.47
Y	9.481395	4.3	40.77	Y	5.557364	4.3	23.89667	Y	7.569767	4.3	32.55	Y	6.125581	4.3	26.34	Y	7.032558	4.3	30.24
Yb	10.89569	0.441	4.805	Yb	6.674225	0.441	2.943333	Yb	8.390023	0.441	3.7	Yb	7.244898	0.441	3.195	Yb	8.14059	0.441	3.59

Table 7a. Concentrations of trace elements from samples of site 1232 and the primitive mantle.

1				2				3				4				5			
Site 1234				Site 1234				Site 1234				Site 1234				Site 1234			
Elements	S/PM	Primitive Mantle	Samples	Elements	S/PM	Primitive Mantle	Samples	Elements	S/PM	Primitive Mantle	Samples	Elements	S/PM	Primitive Mantle	Samples	Elements	S/PM	Primitive Mantle	Samples
Rb	88.81102	0.635	56.395	Rb	71.19685	0.635	45.21	Rb	69.08661	0.635	43.87	Rb	83.73228	0.635	53.17	Rb	87.19685	0.635	55.37
Ba	90.21439	6.6	595.415	Ba	77.78485	6.6	513.38	Ba	70.81136	6.6	467.355	Ba	92.11364	6.6	607.95	Ba	89.71818	6.6	592.14
Th	124.2767	0.0795	9.88	Th	110.1887	0.0795	8.76	Th	95.97484	0.0795	7.63	Th	131.8239	0.0795	10.48	Th	131.4465	0.0795	10.45
Nb	16.13222	0.658	10.615	Nb	12.76596	0.658	8.4	Nb	12.53799	0.658	8.25	Nb	16.50456	0.658	10.86	Nb	15.68389	0.658	10.32
La	53.27932	0.648	34.525	La	44.36728	0.648	28.75	La	40.75617	0.648	26.41	La	52.43827	0.648	33.98	La	53.7037	0.648	34.8
Ce	41.77313	1.675	69.97	Ce	36.08358	1.675	60.44	Ce	32.78209	1.675	54.91	Ce	42.08955	1.675	70.5	Ce	41.33731	1.675	69.24
Sr	5.946734	19.9	118.34	Sr	4.822111	19.9	95.96	Sr	4.524372	19.9	90.035	Sr	5.813065	19.9	115.68	Sr	5.49799	19.9	109.41
Nd	32.112	1.25	40.14	Nd	27.672	1.25	34.59	Nd	24.928	1.25	31.16	Nd	32.664	1.25	40.83	Nd	31.368	1.25	39.21
Zr	23.24333	10.5	244.055	Zr	19.78667	10.5	207.76	Zr	17.99905	10.5	188.99	Zr	24.16286	10.5	253.71	Zr	25.11333	10.5	263.69
Hf	33.78092	0.283	9.56	Hf	28.48057	0.283	8.06	Hf	24.96466	0.283	7.065	Hf	38.09187	0.283	10.78	Hf	36.32509	0.283	10.28
Eu	11.52597	0.154	1.775	Eu	8.766234	0.154	1.35	Eu	8.084416	0.154	1.245	Eu	11.75325	0.154	1.81	Eu	11.03896	0.154	1.7
Gd	16.28676	0.544	8.86	Gd	14.11765	0.544	7.68	Gd	13.09743	0.544	7.125	Gd	17.02206	0.544	9.26	Gd	17.22426	0.544	9.37
Ti	0.289656	1205	349.035	Ti	0.24244	1205	292.14	Ti	0.227444	1205	274.07	Ti	0.282672	1205	340.62	Ti	0.266324	1205	320.92
Dy	15.23739	0.674	10.27	Dy	13.26409	0.674	8.94	Dy	11.5727	0.674	7.8	Dy	15.89021	0.674	10.71	Dy	14.65875	0.674	9.88
Y	13.07791	4.3	56.235	Y	11.10465	4.3	47.75	Y	9.905814	4.3	42.595	Y	13.45116	4.3	57.84	Y	13.90465	4.3	59.79
Yb	15.69161	0.441	6.92	Yb	13.67347	0.441	6.03	Yb	11.90476	0.441	5.25	Yb	15.55556	0.441	6.86	Yb	16.2585	0.441	7.17
6				7				8				9				10			
Site 1234				Site 1234				Site 1234				Site 1234				Site 1234			
Elements	S/PM	Primitive Mantle	Samples	Elements	S/PM	Primitive Mantle	Samples	Elements	S/PM	Primitive Mantle	Samples	Elements	S/PM	Primitive Mantle	Samples	Elements	S/PM	Primitive Mantle	Samples
Rb	90.61417	0.635	57.54	Rb	70.53543	0.635	44.79	Rb	59.33858	0.635	37.68	Rb	92.64567	0.635	58.83	Rb	94.74803	0.635	60.165
Ba	91.37576	6.6	603.08	Ba	74.05	6.6	488.73	Ba	65.63182	6.6	433.17	Ba	96.18788	6.6	634.84	Ba	95.36212	6.6	629.39
Th	126.2893	0.0795	10.04	Th	99.49686	0.0795	7.91	Th	95.22013	0.0795	7.57	Th	135.7233	0.0795	10.79	Th	129.6855	0.0795	10.31
Nb	17.05927	0.658	11.225	Nb	12.68997	0.658	8.35	Nb	10.6231	0.658	6.99	Nb	16.39818	0.658	10.79	Nb	18.88298	0.658	12.425
La	52.99383	0.648	34.34	La	43.41049	0.648	28.13	La	41.7284	0.648	27.04	La	57.80864	0.648	37.46	La	55.61728	0.648	36.04
Ce	44.12239	1.675	73.905	Ce	34.65672	1.675	58.05	Ce	30.92537	1.675	51.8	Ce	43.5403	1.675	72.93	Ce	45.19403	1.675	75.7
Sr	5.464824	19.9	108.75	Sr	4.662814	19.9	92.79	Sr	4.19196	19.9	83.42	Sr	5.765327	19.9	114.73	Sr	6.174623	19.9	122.875
Nd	32.672	1.25	40.84	Nd	27.192	1.25	33.99	Nd	26.176	1.25	32.72	Nd	33.272	1.25	41.59	Nd	33.744	1.25	42.18
Zr	24.4581	10.5	256.81	Zr	19.8981	10.5	208.93	Zr	19.16857	10.5	201.27	Zr	27.36667	10.5	287.35	Zr	25.04524	10.5	262.975
Hf	34.41696	0.283	9.74	Hf	26.39576	0.283	7.47	Hf	28.62191	0.283	8.1	Hf	38.30389	0.283	10.84	Hf	33.99293	0.283	9.62
Eu	10.81169	0.154	1.665	Eu	7.532468	0.154	1.16	Eu	8.571429	0.154	1.32	Eu	10.38961	0.154	1.6	Eu	10.58442	0.154	1.63
Gd	16.80147	0.544	9.14	Gd	12.95956	0.544	7.05	Gd	11.78309	0.544	6.41	Gd	18.36397	0.544	9.99	Gd	16.51654	0.544	8.985
Ti	0.289282	1205	348.585	Ti	0.244083	1205	294.12	Ti	0.2081	1205	250.76	Ti	0.29917	1205	360.5	Ti	0.332079	1205	400.155
Dy	15.25223	0.674	10.28	Dy	11.94362	0.674	8.05	Dy	10.94955	0.674	7.38	Dy	17.80415	0.674	12	Dy	15.32641	0.674	10.33
Y	13.20233	4.3	56.77	Y	10.93488	4.3	47.02	Y	10.69302	4.3	45.98	Y	14.57442	4.3	62.67	Y	13.35116	4.3	57.41
Yb	15.80499	0.441	6.97	Yb	12.9932	0.441	5.73	Yb	11.90476	0.441	5.25	Yb	17.39229	0.441	7.67	Yb	17.04082	0.441	7.515

Table 7b. Concentrations of trace elements from samples of site 1234 and the primitive mantle.

1				2				3				4				5			
Site 1235				Site 1235				Site 1235				Site 1235				Site 1235			
Elements	S/PM	Primitive Mantle	Samples	Elements	S/PM	Primitive Mantle	Samples	Elements	S/PM	Primitive Mantle	Samples	Elements	S/PM	Primitive Mantle	Samples	Elements	S/PM	Primitive Mantle	Samples
Rb	50.50394	0.635	32.07	Rb	44.85039	0.635	28.48	Rb	49.59055	0.635	31.49	Rb	44.48819	0.635	28.25	Rb	59.93701	0.635	38.06
Ba	59.42576	6.6	392.21	Ba	54.01515	6.6	356.5	Ba	57.07803	6.6	376.715	Ba	53.56818	6.6	353.55	Ba	73.13939	6.6	482.72
Th	42.26415	0.0795	3.36	Th	36.47799	0.0795	2.9	Th	39.62264	0.0795	3.15	Th	37.61006	0.0795	2.99	Th	50.9434	0.0795	4.05
Nb	8.715805	0.658	5.735	Nb	7.066869	0.658	4.65	Nb	7.674772	0.658	5.05	Nb	7.264438	0.658	4.78	Nb	9.270517	0.658	6.1
La	23.11728	0.648	14.98	La	20.5787	0.648	13.335	La	20.93364	0.648	13.565	La	19.96914	0.648	12.94	La	25.54012	0.648	16.55
Ce	17.78507	1.675	29.79	Ce	15.92239	1.675	26.67	Ce	16.40597	1.675	27.48	Ce	14.77612	1.675	24.75	Ce	20.8597	1.675	34.94
Sr	7.656533	19.9	152.365	Sr	6.78995	19.9	135.12	Sr	6.987688	19.9	139.055	Sr	6.697487	19.9	133.28	Sr	8.702513	19.9	173.18
Nd	14.62	1.25	18.275	Nd	13.34	1.25	16.675	Nd	12.568	1.25	15.71	Nd	13.52	1.25	16.9	Nd	16.552	1.25	20.69
Zr	9.914286	10.5	104.1	Zr	8.52619	10.5	89.525	Zr	9.066667	10.5	95.2	Zr	8.40381	10.5	88.24	Zr	10.52857	10.5	110.55
Hf	12.49117	0.283	3.535	Hf	11.23675	0.283	3.18	Hf	10.07067	0.283	2.85	Hf	10.81272	0.283	3.06	Hf	12.26148	0.283	3.47
Eu	4.577922	0.154	0.705	Eu	3.824675	0.154	0.589	Eu	4.123377	0.154	0.635	Eu	4.220779	0.154	0.65	Eu	5.25974	0.154	0.81
Gd	6.856618	0.544	3.73	Gd	7.058824	0.544	3.84	Gd	5.744485	0.544	3.125	Gd	6.378676	0.544	3.47	Gd	6.5625	0.544	3.57
Ti	0.144838	1205	174.53	Ti	0.114743	1205	138.265	Ti	0.116432	1205	140.3	Ti	0.117834	1205	141.99	Ti	0.141369	1205	170.35
Dy	5.318991	0.674	3.585	Dy	5.066766	0.674	3.415	Dy	4.836795	0.674	3.26	Dy	4.95549	0.674	3.34	Dy	6.083086	0.674	4.1
Y	5.19186	4.3	22.325	Y	4.510465	4.3	19.395	Y	5.006977	4.3	21.53	Y	4.134884	4.3	17.78	Y	5.427907	4.3	23.34
Yb	5.839002	0.441	2.575	Yb	4.421769	0.441	1.95	Yb	4.705215	0.441	2.075	Yb	4.603175	0.441	2.03	Yb	4.988662	0.441	2.2
6				7				8				9				10			
Site 1235				Site 1235				Site 1235				Site 1235				Site 1235			
Elements	S/PM	Primitive Mantle	Samples	Elements	S/PM	Primitive Mantle	Samples	Elements	S/PM	Primitive Mantle	Samples	Elements	S/PM	Primitive Mantle	Samples	Elements	S/PM	Primitive Mantle	Samples
Rb	59.98425	0.635	38.09	Rb	39.79528	0.635	25.27	Rb	52.85827	0.635	33.565	Rb	59.32283	0.635	37.67	Rb	53.16535	0.635	33.76
Ba	72.6803	6.6	479.69	Ba	44.97576	6.6	296.84	Ba	60.35985	6.6	398.375	Ba	73.18485	6.6	483.02	Ba	61.99848	6.6	409.19
Th	49.43396	0.0795	3.93	Th	28.93082	0.0795	2.3	Th	40.69182	0.0795	3.235	Th	46.03774	0.0795	3.66	Th	35.97484	0.0795	2.86
Nb	9.802432	0.658	6.45	Nb	5.471125	0.658	3.6	Nb	8.381459	0.658	5.515	Nb	9.984802	0.658	6.57	Nb	7.644377	0.658	5.03
La	27.19136	0.648	17.62	La	16.57407	0.648	10.74	La	21.67438	0.648	14.045	La	27.40741	0.648	17.76	La	20.98765	0.648	13.6
Ce	20.79403	1.675	34.83	Ce	14.11343	1.675	23.64	Ce	17.96716	1.675	30.095	Ce	21.8209	1.675	36.55	Ce	17.65373	1.675	29.57
Sr	8.80603	19.9	175.24	Sr	5.352261	19.9	106.51	Sr	7.174121	19.9	142.765	Sr	8.605528	19.9	171.25	Sr	6.972362	19.9	138.75
Nd	16.208	1.25	20.26	Nd	9.976	1.25	12.47	Nd	13.428	1.25	16.785	Nd	16.352	1.25	20.44	Nd	13.472	1.25	16.84
Zr	11.1181	10.5	116.74	Zr	6.664762	10.5	69.98	Zr	9.518095	10.5	99.94	Zr	10.48857	10.5	110.13	Zr	8.492381	10.5	89.17
Hf	14.24028	0.283	4.03	Hf	8.480565	0.283	2.4	Hf	11.59011	0.283	3.28	Hf	14.16961	0.283	4.01	Hf	12.26148	0.283	3.47
Eu	4.805195	0.154	0.74	Eu	3.454545	0.154	0.532	Eu	4.253247	0.154	0.655	Eu	5.064935	0.154	0.78	Eu	4.675325	0.154	0.72
Gd	8.474265	0.544	4.61	Gd	4.191176	0.544	2.28	Gd	5.744485	0.544	3.125	Gd	7.224265	0.544	3.93	Gd	7.536765	0.544	4.1
Ti	0.11805	1205	142.25	Ti	0.078846	1205	95.01	Ti	0.093813	1205	113.045	Ti	0.115212	1205	138.83	Ti	0.099718	1205	120.16
Dy	6.20178	0.674	4.18	Dy	4.080119	0.674	2.75	Dy	5.222552	0.674	3.52	Dy	6.231454	0.674	4.2	Dy	5.311573	0.674	3.58
Y	5.581395	4.3	24	Y	3.146512	4.3	13.53	Y	4.653488	4.3	20.01	Y	5.518605	4.3	23.73	Y	4.411628	4.3	18.97
Yb	6.780045	0.441	2.99	Yb	3.809524	0.441	1.68	Yb	4.68254	0.441	2.065	Yb	4.965986	0.441	2.19	Yb	4.557823	0.441	2.01

Table 7c. Concentrations of trace elements from site 1235 and the primitive mantle.

APPENDIX I

Major element concentrations are collected from the EDS and are measured in weight percent. The standards used are Basalt, Hawaiian Volcanic Observatory (BHVO-2) and Rhyolite, Glass Mountain (RGM-2).

Site Averages				Standards	
M. E.	1232	1234	1235	Gl Rhyolite	BHVO-2
Na2O	3.59761	5.2184	3.85834	3.3946809	2.2045
MgO	0	0	0.0796	0	6.5935
Al2O3	12.9602	13.8119	13.3248	12.094158	12.6035
SiO2	75.9135	71.4934	78.1255	77.46383	45.3415
P2O5	0	0	0.01265	0	0
K2O	4.91191	2.93951	2.18082	4.8595628	0.8705
CaO	0.57741	1.51162	1.58134	0.4853659	14.8575
TiO2	0.1835	0.29002	0.15638	0.0822581	2.9705
MnO	0.04563	0.04723	0.05199	0.0177628	0.3205
FeO Total	1.01468	3.52637	1.51133	1.3597122	14.2385

Table 8. Average of readings of all major element concentrations and standards.